

JADES: Differing assembly histories of galaxies - Observational evidence for bursty SFHs and (mini-)quenching in the first billion years of the Universe

Tobias J. Looser^{1,2,*}, Francesco D'Eugenio^{1,2}, Roberto Maiolino^{1,2,3}, Sandro Tacchella^{1,2}, Mirko Curti^{4,1,2}, Santiago Arribas⁵, William M. Baker^{1,2}, Stefi Baum⁶, Nina Bonaventura^{7,8,9}, Kristan Boyett^{10,11}, Andrew J. Bunker¹², Stefano Carniani¹³, Stephane Charlot¹⁴, Jacopo Chevallard¹², Emma Curtis-Lake¹⁵, A. Lola Danhaive^{1,2}, Daniel J. Eisenstein¹⁶, Anna de Graaff¹⁷, Kevin Hainline⁹, Zhiyuan Ji⁹, Benjamin D. Johnson¹⁶, Nimisha Kumari¹⁸, Erica Nelson¹⁹, Eleonora Parlanti¹³, Hans-Walter Rix¹⁷, Brant Robertson²⁰, Bruno Rodríguez Del Pino⁵, Lester Sandles^{1,2}, Jan Scholtz^{1,2}, Renske Smit²¹, Daniel P. Stark¹⁸, Hannah Übler^{1,2}, Christina C. Williams²², Chris Willott²³, and Joris Witstok^{1,2}

(Affiliations can be found after the references)

ABSTRACT

We use deep NIRSpec spectroscopic data from the JADES survey to derive the star formation histories (SFHs) of a sample of 200 galaxies at $0.6 < z < 11$ and spanning stellar masses from 10^6 to $10^{9.5} M_\odot$. We find that galaxies at high-redshift, galaxies above the Main Sequence (MS) and low-mass galaxies tend to host younger stellar populations than their low-redshift, massive, and below the MS counterparts. Interestingly, the correlation between age, M_* and SFR existed even earlier than Cosmic Noon, out to the earliest cosmic epochs. However, these trends have a large scatter. Indeed, there are examples of young stellar populations also below the MS, indicating recent (bursty) star formation in evolved systems. We explore further the burstiness of the SFHs by using the ratio between SFR averaged over the last 10 Myr and averaged between 10 Myr and 100 Myr before the epoch of observation ($\text{SFR}_{\text{cont},10}/\text{SFR}_{\text{cont},90}$). We find that high-redshift and low-mass galaxies have particularly bursty SFHs, while more massive and lower-redshift systems evolve more steadily. We also present the discovery of another (mini-)quenched galaxy at $z = 4.4$ (in addition to the one at $z=7.3$ reported by Looser et al. 2023), which might be only temporarily quiescent as a consequence of the extremely bursty evolution. Finally, we also find a steady decline of dust reddening of the stellar population approaching the earliest cosmic epochs, although some dust reddening is still observed in some of the highest redshift and most star forming systems.

Key words. Galaxies: high-redshift, formation, evolution, stellar content, star formation, statistics

1. Introduction

Understanding the nature and characteristics of stellar populations and the assembly histories of their host galaxies is a key objective in modern astrophysics. Stellar populations offer a unique window into the early universe, providing insights into the formation and evolution of galaxies, as well as shedding light on the processes that shaped the cosmos as we know it today.

The launch of the James Webb Space Telescope (*JWST*, Gardner et al. 2006, 2023), with its unparalleled capabilities, ushers in a new era of astronomical exploration, providing the opportunity to uncover the intricate characteristics of stellar populations in objects at redshifts previously unattainable. The spectroscopic capabilities of the Near Infrared Spectrograph (NIRSpec, Jakobsen et al. 2022) onboard *JWST* and its high sensitivity, enable us to push to fainter, lower mass and more distant sources and measure their properties accurately. With *JWST*, we can explore the early stages of galaxy formation and trace the evolution of stellar populations across cosmic time.

Stellar populations are a crucial tool to understand the assembly of galaxies, as their past star-formation histories (SFHs) are imprinted in their stellar record. Hence, they encode valuable information about the various physical mechanisms which shaped their past star formation activity, such as stellar winds, feedback from supernovae (SN) and Active Galactic Nuclei (AGN), inter-

actions and mergers, or environment. It is now widely thought, as predicted by numerical simulations (Kawata & Gibson 2003; Ceverino et al. 2021; Dome et al. 2023) and emerging observational evidence Caputi et al. (2007); Smit et al. (2014, 2015); Díaz-Santos et al. (2017); Endsley et al. (2021, 2022), that these mechanisms can make SFHs "bursty", particularly in the early Universe (Faucher-Giguère 2018; Tacchella et al. 2016) and in low-mass systems (Weisz et al. 2012a; Tacchella et al. 2020a). Here "burstiness" refers to patterns of star formation characterized by episodic bursts of intense activity interspersed with "lull" phases, i.e. phases during which the galaxy is forming significantly fewer stars at the epoch of observation (~ 10 Myr time-scale) than during its recent past (~ 100 Myr time-scale), and potentially even quiescent periods, so-called mini-quenching events (Dome et al. 2023; Gelli et al. 2023). Mini-quenching events refer to the state of a galaxy in which star formation is temporarily halted or strongly suppressed, i.e. $s\text{SFR} < 0.2/t_{\text{obs}}$, likely because the inflow of gas into the galaxy is disrupted, leading to a temporary halt of star formation activity. Unlike long-term quenching processes that lead to a permanent decline in star formation, mini-quenching events are transient and typically last for only a few tens to a hundred million years.

Studying bursty SFHs and mini-quenching is therefore crucial for understanding the diversity of galaxy properties and the underlying physical processes that shape them. The timing, duration, and intensity of star formation bursts can influence the overall stellar mass assembly, the enrichment of heavy elements, and

* tj154@cam.ac.uk

the morphological evolution of galaxies. Further, bursty SFHs are likely connected to the growth of supermassive black holes and the feedback mechanisms associated with AGN, even in low-mass systems (Koudmani et al. (2019)). Hence, the investigation of burstiness in SFHs of galaxies provides important constraints for theoretical models and is essential for constructing a comprehensive picture of galaxy evolution and unravelling the intricate processes that drive the diverse range of galaxy properties observed in the universe.

However, despite being thought to be a common phenomenon in galaxy evolution, observational evidence for bursty SFHs and mini-quenching is to date still sparse, mainly due to (pre-*JWST*) instrumental limitations. Identifying and characterizing bursty SFHs requires high signal-to-noise (S/N) data, to disentangle the different star formation episodes within a galaxy. Observationally, we (obviously) cannot know the future of any particular galaxy. Hence, it is difficult to assess on what time-scales, if not permanently, a particular galaxy remains quenched - making it observationally difficult to differentiate between mini-quenching and permanent-quenching on a galaxy-by-galaxy basis. Nonetheless, data on molecular cold gas in or around the galaxy, or evidence for infalling giant clouds of cold gas, could give important clues on whether the galaxy will obtain new fuel for star formation in the near future. Hence, unless such information is available for any particular galaxy we observe in a quiescent phase, we can only speculate about the duration over which the galaxy remains quenched; so we propose to call these objects (mini-)quenched, to indicate that it is likely that they will re-ignite again in its future, particularly for high-redshift or low-mass systems; but also leaving open the possibility that they continue to have a very low specific SFR (sSFR) over extended time-scales, or remain permanently quenched.

In order to unambiguously establish mini-quenching observationally, rejuvenating galaxies characterised by old stellar populations and UV-faintness while exhibiting strong nebular emission lines tracing recent star formation, have yet to be observed. Additionally, more galaxy spectra are needed to identify galaxies in different phases of their burstiness cycles: from "bursts" via "regular", and "lull" phases (see e.g. the post-starburst, nearly quiescent galaxy in Strait et al. (2023)), to mini-quenching and rejuvenating galaxies, to provide constraints on the physical processes shaping the burstiness of SFHs. Until such large data sets are obtained we propose to refer to these types of quiescent galaxy, which might re-ignite soon again in the future like the one presented in Looser et al. (2023), as (mini-)quenched, as argued above.

Large statistical samples are needed to characterize burstiness, (mini-)quenching events and the associated duty cycles as a function of different galaxy population properties, such as observed redshift, stellar mass M_* or distance from the main sequence (MS).¹ Leaving the burstiness of high-redshift and low-mass galaxies - and the physics which shapes it - as one of the major unknowns in galaxy assembly and evolution to date; and one of the key science goals for *JWST*.

In this paper, we present a first study of stellar populations in high redshift galaxies and present observational results on the burstiness of SFHs as a function of stellar mass and redshift; and further observational evidence for (mini-)quenching events at high redshift. This work is based on data acquired by our *JWST* Advanced Deep Extragalactic Survey (JADES, Eisenstein et al., in prep.) survey. JADES is a large *JWST* GTO program,

formed out of a collaboration between the NIRSpec (Jakobsen et al. 2022) and NIRCам (Rieke et al. 2023) instrument science teams, combining both imaging and spectroscopy. The program is designed to present an unprecedented study of the physical properties of galaxies at high redshift, mostly focusing on targets beyond the Cosmic Noon.

The paper is structured as follows: In section 2 we present our JADES data, in particular the NIRSpec PRISM spectra, summarize the data processing and describe our full spectral fitting methodology based on PPXF (Cappellari 2017, 2022). In section 3 we discuss our observational results about the stellar ages and stellar dust attenuation in different bins of characteristic galaxy properties. In section 4 we present our results on the burstiness of SFHs. In section 5 we discuss our results. In section 6 we summarize the key findings of this paper.

Throughout this work, we assume a Chabrier (Chabrier 2003) initial mass function (IMF) and a Λ CDM cosmology with the following parameters: $H_0 = 70 \text{ km s}^{-1} / \text{Mpc}$, $\Omega_M = 0.3$ and $\Omega_\Lambda = 0.7$.

2. Data, data reduction and extraction of basic physical quantities

The NIRSpec (Jakobsen et al. 2022) micro-shutter array (MSA, Ferruit et al. 2022) spectra used in this work were obtained as part of our JADES GTO program (PI: N. Lützgendorf, ID:1210) observations in the Great Observatories Origins Deep Survey South field (GOODS-S, Giavalisco et al. (2004)) between October 21–25, 2022. These spectra constitute the HST-DEEP tier of the survey (hereafter: JADES/HST-DEEP) and were obtained using the disperser/filter configuration PRISM/CLEAR, which covers the wavelength range between $0.6 \mu\text{m}$ and $5.3 \mu\text{m}$ and provides spectra with a nominal wavelength-dependent spectral resolution of $R \sim 30\text{--}330$ (Jakobsen et al. 2022)².

The program observed a total of 253 galaxies over three dither pointings. For each target, three microshutters are simultaneously opened for exposure. Each dither pointing uses a different MSA configuration to place the spectra at different positions on the detector - to decrease the impact of detector gaps, mitigate detector artefacts and improve the signal-to-noise ratio (S/N) for high-priority targets, while increasing the density of observed targets. Within each individual dither, the exposure is three-pointing nodded along the slit. Each three-point nodding was integrated for 8403 seconds. The three-nod pattern has been repeated four times. Each target was observed in either one or multiple pointings, resulting in a total exposure time of up to 28 hours for the prism.

The flux-calibrated spectra were extracted using pipelines developed by the ESA NIRSpec Science Operations Team (SOT) and the NIRSpec GTO Team. A detailed description of the pipelines will be presented in a forthcoming NIRSpec/GTO collaboration paper (Carniani et al., in prep.). For a more detailed presentation of the JADES/HST-DEEP spectra and a discussion of the sample selection we refer to Bunker et al. (subm.). In this paper, we use all spectra for which a redshift could be established. For the galaxies with strong emission lines, we use the same redshifts as those presented in Bunker et al. (in prep.). Otherwise, we use redshifts inferred from visual inspection of the continuum and weaker lines, which are further refined by PPXF, see below.

¹ Where MS describes the positive scaling relation between M_* and SFR of the star-forming galaxy population (Sandles et al. 2022, e.g.).

² For a sub-sample of targets, also higher-resolution grating spectra were obtained as a part of this program. However, we focus on the prism spectra in this work, which are more relevant for the stellar continuum.

We remark that with the effective slit width of 0.2 arcsec, the JADES spectra suffer from wavelength-dependent aperture losses. This is corrected assuming a point-source geometry, which leads to systematic underestimate of the flux for the most extended, lowest-redshift sources.

2.1. Full spectral fitting with PPXF

The R100 spectra are fitted with a methodology based on the χ^2 -minimization Penalized PiXel-Fitting code³ PPXF (Cappellari 2017, 2022), leveraging bootstrapping to infer key physical quantities (Looser et al., *subm.*). To fit the stellar continuum, a library of simple stellar-population (SSP) templates, coupled with a Calzetti et al. (2000) dust attenuation law (but without any additive or multiplicative polynomials), are fitted as a (non-negative) linear superposition to the continuum spectrum. The SSP library uses synthetic model atmospheres from the C3K library (Conroy et al. 2019) with a resolution of $R=10,000$, adopting the MIST isochrones of Choi et al. (2016), solar abundances and a Salpeter IMF. Throughout the paper, we change the IMF to Chabrier, using the formula of Speagle et al. (2014). The synthetic SSP spectra span the 2D age-metallicity logarithmic grid from $\text{age}_{\text{SSP}} = 10^{6.0}$ yr to $10^{10.3}$ yr and $[\text{M}/\text{H}] = -2.5$ to 0.5. For each galaxy, we cut the age grid to be consistent with the age of the Universe at that redshift, plus a buffer of a single bin⁴. For a self-consistent treatment of nebular emission lines, we use Gaussians to fit them simultaneously with the stellar continuum – the SSP models themselves do not include nebular emission.

We describe below in detail the method based on the PPXF algorithm applied to each JADES/HST DEEP spectrum in this work:

1. First, the C3K templates are convolved to match the wavelength-dependant spectral resolution of the spectrum. Secondary to wavelength, the effective spectral resolution (R) depends on the degree of ‘slit filling’, i.e. the ratio between the galaxy size and the 0.2-arcsec width of the micro shutters. This effect is estimated to be as large as a factor of two. To enable PPXF to reproduce the data, we artificially increase R for all targets.
2. Both the spectrum and the templates are re-normalized by the median flux per spectral pixel in the spectrum to avoid numerical issues, and to enable the use of regularization in PPXF (‘regul’ keyword), allowing to penalize non-smooth weight distributions (see Cappellari 2017 for more details).
3. A first fit with $\text{regul}=5$ is used to obtain an initial estimate of the model and remove outliers using $4\text{-}\sigma$ clipping.
4. Then we perform a wild bootstrapping by perturbing the spectrum S with the estimated noise spectrum from the data reduction N : $S^*(\lambda) = S(\lambda) \pm N(\lambda')$, where $N(\lambda')$ is randomly chosen from the noise spectrum within ± 50 pixels for each spectral pixel λ .
5. We fit the perturbed spectrum $S^*(\lambda)$ again with PPXF, again with $\text{regul}=5$.
6. We repeat steps 4&5 one hundred times.
7. This method probes the sampling distribution of each individual SSP grid weight. The 100 bootstrapped grids of SSP weights are then averaged to recover a non-parametric SFH consistent with the intrinsic noise of the spectrum.

The output is a reconstructed assembly history of the target under consideration, as traced by this “archaeological” approach using the observed remaining stellar populations as the “fossil record” of the system. Due to the point-source assumption in the data reduction, our spectra do not capture the absolute M_\star and SFR of each galaxy, leading to values that are systematically underestimated. In addition, by modelling the spectra alone (i.e., without photometry), we neglect any light falling outside the MSA shutters; in particular, colour gradients and clumpy morphologies cannot be captured by our approach. However, we remark that the impact of this effect is strongest where it is least relevant to our conclusions, i.e. in the lowest redshift bin and at the highest stellar masses.

The distinctive advantage of our approach is that, by fitting the observed spectra with a superposition of independent SSPs and gas templates, we are not imposing a particular parametric SFH or a single metallicity on the spectrum. In other words, our recovered SFHs are non-parametric and do not depend on any assumption about the underlying physics of galaxy evolution. Crucially, any recovered scaling relation cannot have been introduced by parametric assumptions about the shape of our fitted SFHs. As an example, the fitted light-weighted 2D grid of SSP-weights, and the conversion of these weights into a non-parametric SFH for the spectra presented in Fig. 1 is shown in Figs. A.1&A.2.

While this non-parametric astro-archaeological approach is extremely powerful, the analysis of its outputs has to be done with utmost care. This method has been tested on data from the local MaNGA (Bundy et al. 2015) survey, and has been shown to recover meaningful average star-formation and chemical-evolution histories (Looser et al., *submitted*).

Focusing on the NIRSpect PRISM spectra, while the recovered ages, traced by the UV-slope, the Balmer break and the overall shape of the spectrum can be recovered reliably, the spectral resolution of the spectra may not be sufficient to reliably estimate the metallicity of the underlying galaxy populations. Due to the well known age-metallicity degeneracy, and known and unknown systematics, such as dust obscuration, or flux calibration issues, we can trust returned SSP weights to different degrees. To assess the stability of the SSP weights, the bootstrapping methodology described above is highly instructive, as it returns a scatter distribution for each individual SSP weight, as well as for any quantity derived from the weight grid. The tests reveal that ages are reliable in conservative 1 dex bins in $\log_{10}(\text{Age}[\text{yr}])$, from $\log_{10}(\text{Age}[\text{yr}]) = 6.0$ to 10.0. Hence, for this paper, we bin the SSP weight-grid, as presented in Fig. A.2, into four age bins, as presented below, see Fig. 3–5.

2.2. Stellar mass

To measure the stellar mass M_\star for each galaxy, we sum the individual weights of the mass-weighted SSP grid fitted with PPXF. To test the reliability of the PPXF masses, we compare them to masses inferred from the BEAGLE code (Chevallard & Charlot 2016) for the same data set, presented in Curti et al. (2023) and Chevallard et al. (*in prep.*). The PPXF masses and the BEAGLE masses show a strong correlation with an RMS-scatter of 0.2 dex, however we note an offset of 0.2 dex. Even though the two codes infer different masses for some galaxies, the general agreement means that our choice of M_\star does not drive the results presented in this paper. A comparison between the PPXF and BEAGLE masses is presented in Appendix B.

³ <https://pypi.org/project/ppxf/>; version 8.1.0

⁴ These SSP templates are available from the author C. Conroy upon reasonable request.

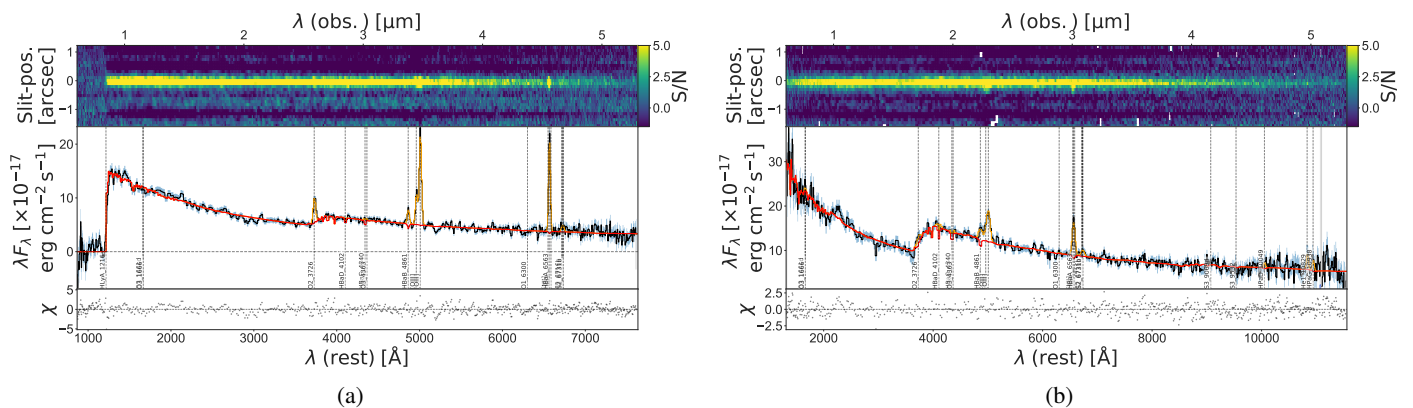


Fig. 1: Left: Example of a JADES-DEEP spectrum of a star-bursting galaxy at redshift $z = 5.9$. Right: Example of a JADES-DEEP spectrum of a weakly star-forming galaxy at redshift $z = 3.6$. The noise is indicated by the blue shaded regions. The fitted PPXF continuum is given in red, the nebular emission lines in yellow. The vertical dashed lines mark the rest-frame wavelengths of strong nebular emission lines. The upper panel shows the S/N of the combined 2D spectrum (note that the 1D spectrum is not extracted from the combined 2D spectrum). The bottom panel indicates the reduced residuals of the fit.

2.3. SFR from nebular Balmer lines

To calculate the star-formation rate (SFR) from nebular emission lines, we follow a similar method as Curti et al. (2023). We apply the calibration of Kennicutt & Evans (2012), using the attenuation-corrected $H\alpha$ luminosity where available, i.e. at $z \leq 7$, and $2.86 \times H\beta$ otherwise. The dust-attenuation correction is based either on the Balmer decrement ($H\alpha/H\beta = 2.86$ or $H\beta/H\gamma = 0.47$; where both lines are detected) adopting a Gordon et al. (2003) dust correction; or on the $E(B-V)$ from full spectral fitting, where only one Balmer line was detected.

Fig. 2 shows the SFR-mass plane in three different redshift bins. The blue lines represent simple linear fits to the star forming main sequence (MS) for this particular sample in the three redshift ranges. The fit likely overestimates the true MS due to complex selection effects. A more careful analysis of the MS, taking selection bias into account is beyond the scope of this work. Further, for the lowest, middle and highest redshift in each of the three redshifts bin, we plot the redshift-dependent quenching threshold $sSFR < 0.2/t_{\text{obs}}$, where $t_{\text{obs}}(z)$ is the age of the Universe as a function of redshift (e.g. Gallazzi et al. 2014; Pacifici et al. 2016; Carnall et al. 2023). The quenching-threshold redshifts are $z = 0, 1, 2$ for the lowest redshift bin (colored in orange, green and red, respectively); $z = 2, 3.5, 5$ for the middle redshift bin; and $z = 5, 8, 11$ for the highest redshift bin.

3. Results: Stellar populations

In this section, we present the results of our non-parametric full spectral fitting with PPXF on the inferred stellar population properties.

3.1. Stellar ages as a function of M_* , Δ_{MS} and redshift z

In Fig. 2, individual galaxies are color-coded by their mass-weighted stellar ages. As one expects, with increasing redshift the average ages of the galaxies decrease. Further, we observe interesting trends with M_* and Δ_{MS} : (a) High-mass galaxies tend to be overall older than low-mass galaxies in all redshift bins (in agreement with recent studies at Cosmic Noon, e.g. Carnall et al. (2019b); Tacchella et al. (2022); Ji & Giavalisco (2022)), although there is considerable variation; (b) at fixed stellar mass, galaxies above the MS (as traced by nebular emission lines on

10 Myr time-scales) are younger than galaxies below the MS. This indicates that the Δ_{MS} of a galaxy at the epoch of observation is to some extent correlated with its past formation history over longer time-scales. However, there is significant variation. The interesting question is whether this is due to measurement uncertainties or bursty SFHs, as will be discussed below.

3.2. Stacked SFHs

In Fig. 3-5 the SFHs of individual galaxies are combined together to provide a composite view. The individual SFHs are stacked in three z , M_* and Δ_{MS} bins, as indicated by the labels. We re-iterate that the individual PPXF SSP-grid fits are non-parametric: PPXF can freely choose the weighting of each individual SSP spectrum given, without any assumption on the functional form of the SFH. The stack in each bin are constructed as follows. First, for each galaxy, the SSP weights are normalized by the total sum of SSP-weights, i.e. we construct a "relative" weight-distribution of SSPs. These normalized weights are then averaged (i.e. each galaxy contributes equally) over all galaxies in a given z - M_* - Δ_{MS} bin. The inferred SSP-weight grids are then averaged over four log-age bins with width of 1 dex. This facilitates the identification of relative trends, and our bootstrapping tests indicate that the inferred grid weights cannot not be trusted on a finer age sampling.

The stacked SFHs reveal interesting patterns in the SFHs of different galaxy populations in the sample as a function of z , M_* and Δ_{MS} , similar to those found for more massive galaxies around the Cosmic Noon (Ji & Giavalisco 2023). As one expects, low-redshift galaxies exhibit older populations, with more stellar mass formed at large look-back times. Conversely, high-redshift galaxies are mostly dominated by young stellar populations. Within each redshift bin, there are also interesting trends with Δ_{MS} and M_* : Galaxies below the MS tend to have significantly more contribution of old SSPs than galaxies on the MS, while galaxies above the MS exhibit the highest mass fraction of young SSPs. Additionally, there is a weak trend with M_* : massive galaxies tend to be older than low-mass galaxies.

However, a very interesting finding is that even in the highest redshift bin there is a substantial contribution by evolved (old) stellar populations (formed more than one Gyr before the epoch of observation), indicating that the SFH analysis is revealing the

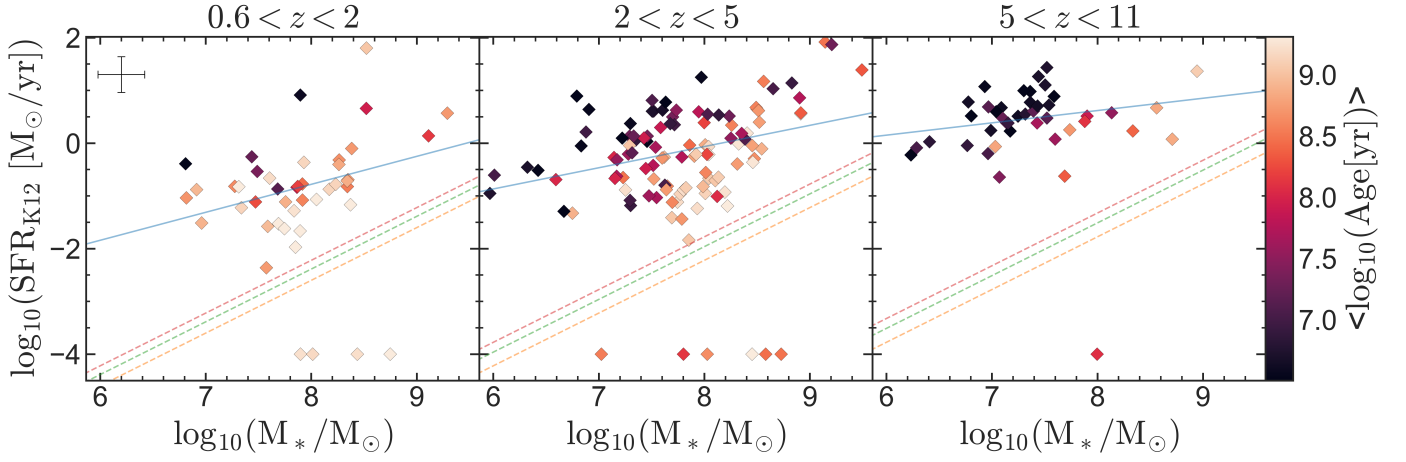


Fig. 2: SFR-mass plane color-coded by the average mass-weighted stellar ages measured by PPXF in three different redshift bins. Each data-point represents a single galaxy. The blue lines represent a simple linear fit of the star-forming main sequence (MS) for this sample at that redshift bin. For reference, the three dotted lines indicate the quenched threshold for the lowest, middle and highest redshifts in each subplot, see main text. The error bar in the top-left corner represent the RMS-errors for M_* and SFR for the entire sample. Quiescent and (mini-)quenched galaxies, for which no SFR could be estimated due to non-detection of the relevant nebular emission lines, are plotted at the bottom of the three sub-figures.

imprint of the earliest episodes of star formation of these systems. However, we caution that inferring the oldest stellar populations in these system is quite difficult, as they contribute little to the stellar light, hence this finding should be confirmed with additional data.

3.3. Dust attenuation as a function of M_* , Δ_{MS} and redshift z

Fig. 6 shows the SFR-mass planes color-coded by E(B-V), tracing the amount of reddening of the stellar continuum caused by interstellar dust along the line of sight, as fitted with PPXF. The galaxies are divided into the same three redshift bins as in section 3.1. We observe a clear trend with Δ_{MS} : Spectra of quiescent galaxies and galaxies below the MS exhibit less dust attenuation, while particularly star-bursting galaxies exhibit significant reddening (see also Sandles et al., in prep.). Additionally, there is a trend with M_* : massive galaxies tend to be dustier than low-mass galaxies. Finally, the dust reddening declines at the highest redshift (at a given stellar mass and SFR), although most galaxies in the highest redshift bins still exhibit the presence of some, but moderate amounts of dust, especially in the more star-forming and massive systems. In the two lower-redshift bins, most galaxies below the MS exhibit no dust at all, while particularly high-mass, star-bursting galaxies above the MS show significant dust reddening of the stellar continuum. Overall, we recover the mass dependence observed in the local Universe and at low redshift (e.g., Pannella et al. 2009; Whitaker et al. 2017; McLure et al. 2018; Shapley et al. 2022; Maheson et al. 2023), but also show a clear dependence on the SFH and/or redshift.

3.4. SFR from stellar populations

In Fig. 7 we present results on the inference of SFR_{cont} over different time-scales directly from the stellar populations and compare this to SFR estimated from nebular emission lines ($SFR_{neb,10}$), see section 2.3, where SFR_{cont} is derived via the fitting of the stellar continuum with PPXF; and averaged over 10 Myr ($SFR_{cont,10}$, left) and 100 Myr ($SFR_{cont,100}$, right), respectively.

We find excellent agreement between $SFR_{cont,10}$ traced by the stellar continuum, and $SFR_{neb,10}$ traced by the optical Balmer lines. The small difference in normalisation might be partially explained by the assumption of solar metallicity in K12, which overestimates the SFR in metal-poor systems. A comparison between K12 and metallicity calibrated SFR, see e.g. Shapley et al. (2023), will be presented in a forthcoming work; for this study, we focus on the mean trend and its scatter, therefore we ignore the systematic offset.

The right panel of Fig. 7 shows a strong correlation between $SFR_{cont,100}$ and $SFR_{neb,10}$, although there is more scatter, and we observe a deviation in the normalization.

The interesting question is whether the scatter is due to physical variation in SFR, i.e. bursty SFHs, or due to measurement uncertainties. Moreover, the difference in overall normalization may be due to selection bias, i.e. we preferentially observe galaxies in "star-bursting" phases, as they are much brighter, both in nebular emission line luminosities and UV continuum luminosity. We will present observational evidence that a significant part of the scatter is physical, indicating bursty SFHs particularly at high-redshift and in low-mass systems, in the next section.

4. Results: Observational evidence for bursty SFHs

In this section, we present observational results indicating bursty SFHs in high-redshift and low-mass systems. Specifically, in addition to the star-bursting galaxy in Fig. 1a, we show examples of galaxies in "regular" phases, i.e. galaxies which formed stars at roughly the same rate over the last 10 Myr as over the last 100 Myr; galaxies in "lull" phases, i.e. galaxies which formed significantly fewer stars over the last 10 Myr relative to the last 100 Myr, but with detected Balmer lines associated with recent star-formation activity and above the quenched-threshold ($sSFR \geq 0.2/t_{obs}$). More broadly, we present an analysis of burstiness as a function of redshift z and in the SFR-mass plane. Furthermore, we present the discovery of an additional, low-mass (mini-)quenched galaxy in a quiescent phase at high redshift. Finally, we also discuss observational biases.

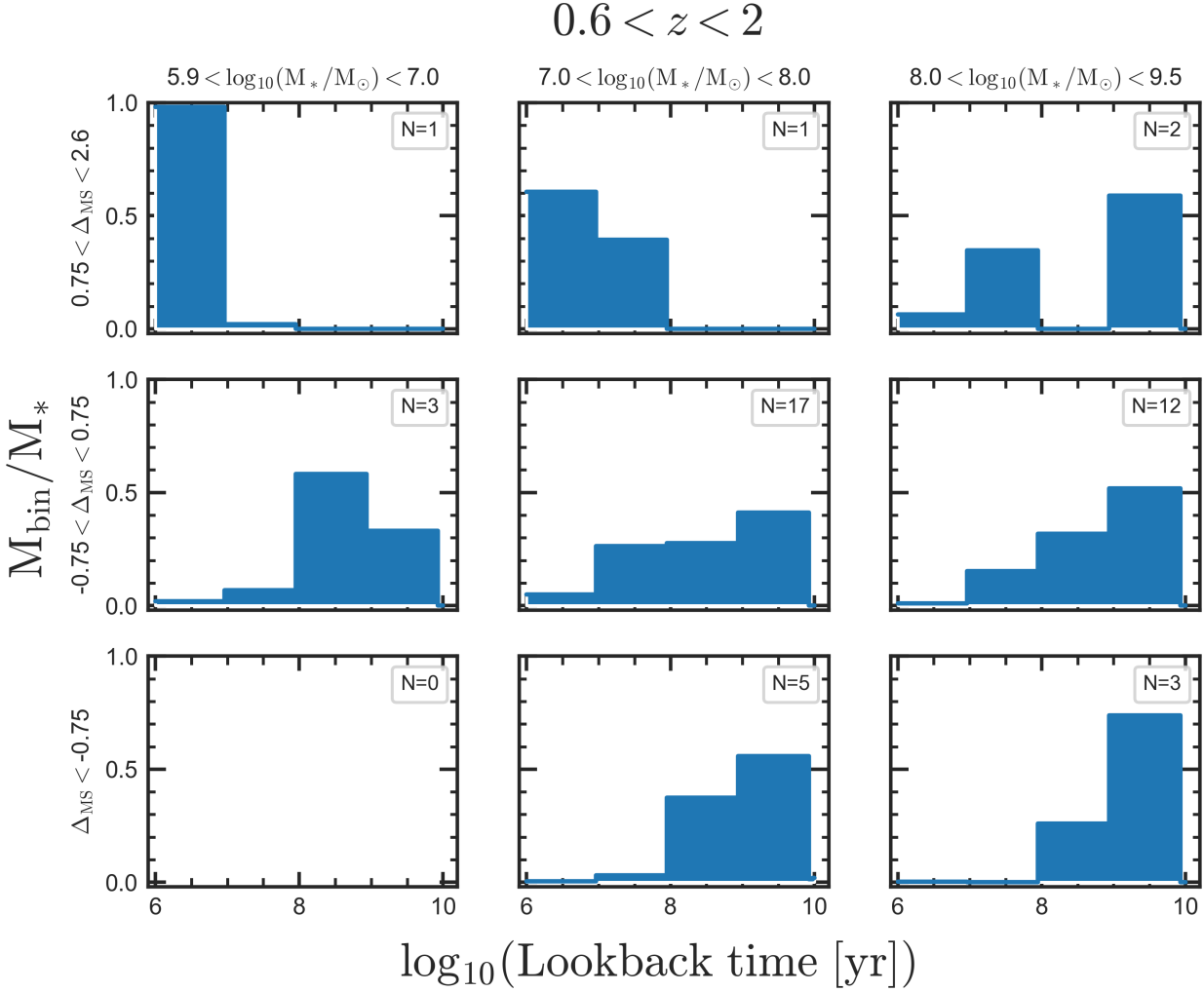


Fig. 3: Mass-weighted stacks of "normalized" SFHs of galaxies in three bins of each, M_* and Δ_{MS} , in the redshift range $0 < z < 2$. The number in the legend of each sub-figure indicates the number of galaxies contributing to the stack. In each bin, the SSP-weights of each contributing galaxy are first normalized, and then averaged over all galaxies contributing to the bin. The underlying inferred SSP weight-grid is collapsed into four age-bins, where each bin has a width of 1 dex, as indicated. The oldest bin (from 1 Gyr to 10 Gyr) is artificially extended for consistent plotting: For each individual galaxy SFH, only SSP templates consistent with the age of the Universe at the redshift of the target are included in the fitting. See section 2.1 for more details.

4.1. Examples of galaxies in "lull" or "regular" phases at high- z

Fig. 8 shows two examples of observed JADES/HST-DEEP galaxies in a "lull" and a "regular" phase, respectively, in the intermediate-redshift bin. Although both spectra are blue with a steep UV slope, indicating strong star formation over the past ~ 100 Myr, the nebular emission lines are low-luminosity, indicating lower star-formation activity over the last ~ 10 Myr before the epoch of observation for the galaxy in Fig. 8a, and a regular star-formation activity over the last 10 Myr in the galaxy in Fig. 8b. The regular galaxy shows low EW emission in $H\beta$, [OIII] and $H\alpha$, for these redshifts. The lulling galaxy show even lower EW, particularly in $H\alpha$, and no detection of $H\beta$. The first one shows only a very weak Balmer break whereas in the latter an already quite strong Balmer break is emerging. This further supports the interpretation of these galaxies as "in a regular" phase and "in a lull" phase.

4.2. Burstiness as a function of redshift z and M_*

Fig. 9 shows the $(SFR_{neb,10})$ -mass planes color-coded by the ratio $SFR_{cont,10}/SFR_{cont,90}$, i.e. the ratio between the SFR averaged over the last 10 Myr and the SFR averaged between 10 to 100 Myr. The data is divided in the three redshift bins, as indicated. Both, $SFR_{cont,10}$ and $SFR_{cont,90}$ are inferred with stellar population fitting with PPXF. The reason for using $SFR_{cont,90}$ is that it is estimated from a distinct set of weights in the SSP-grid, i.e. we avoid correlation by construction.

The ratio between the two PPXF SFR tracers over different time-scales indicates whether a single galaxy is in a "burst", a "regular" or a "lull" phase at the epoch of observation. Studying the variation of this ratio between galaxies with otherwise similar properties provides important evidence for the burstiness of this galaxy population.

A complementary perspective, and important validation, of our observational evidence for the variation of star-formation burstiness with redshift z and M_* is presented in Fig. 10. Galaxies in "regular" phases are indicated by green colors; galaxy

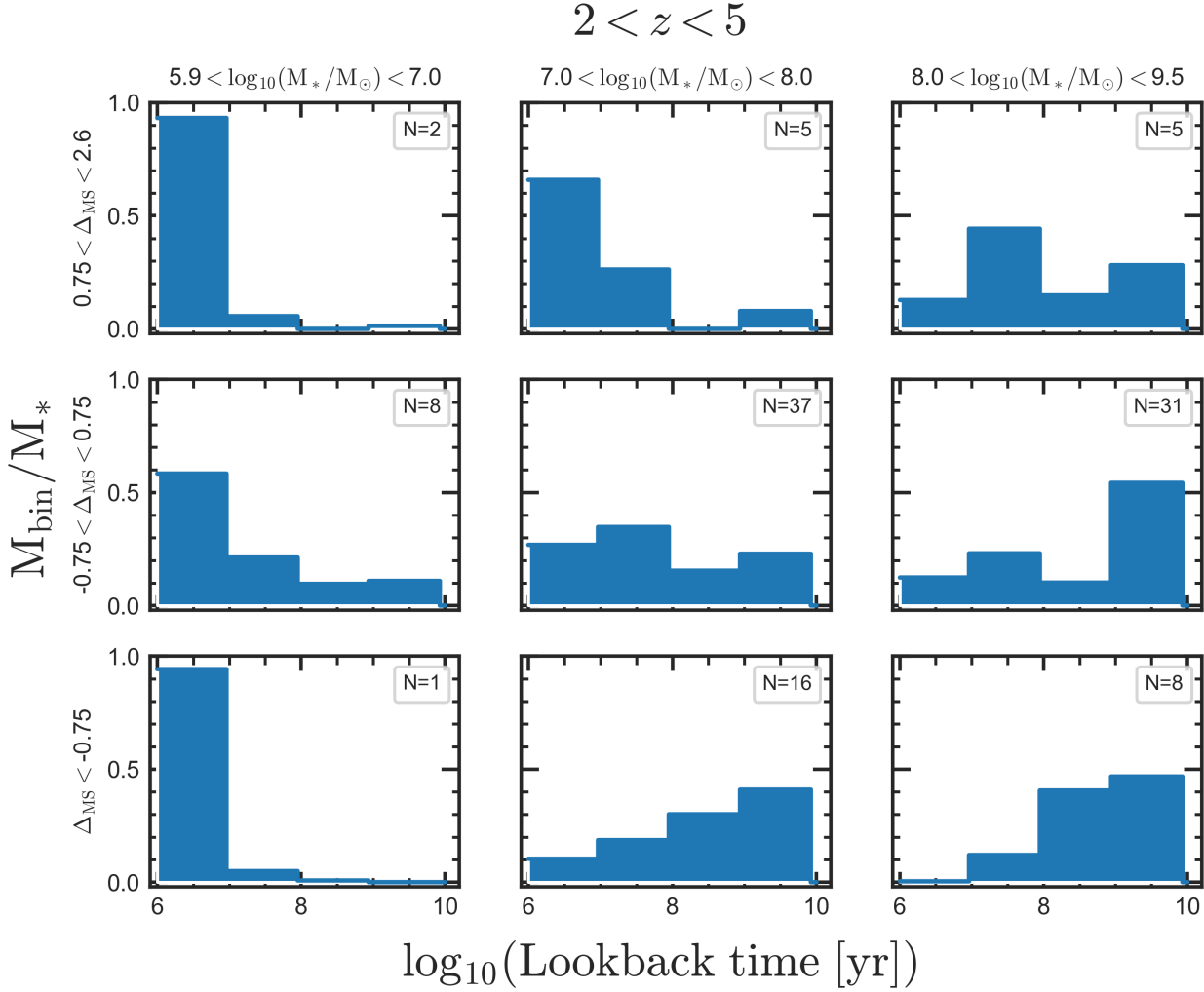


Fig. 4: Mass-weighted stacks of "normalized" SFHs of galaxies in three M_* and Δ_{MS} bins in the redshift bin $2 < z < 5$. The number in the legend of each sub-figure indicates the number of galaxies contributing to each stack. See Fig. 3 and section 2.1 for more details.

in burst phases by light colors; galaxies in lulls in dark colors, and (mini-)quenched or permanently quenched galaxies in black. Here we investigate burstiness by looking at the ratio of $\text{SFR}_{\text{neb},10}$ and $\text{SFR}_{\text{cont},100}$ (see left plot). The right plot shows $\text{SFR}_{\text{cont},10}/\text{SFR}_{\text{cont},90}$, as in Fig. 9. These results are consistent with the results presented above: it is evident that the low-mass and high-redshift galaxy populations are burstier, while the high-mass and low-redshift populations exhibit more galaxies in "regular" phases. As described above, in the low-mass and high-redshift populations, we predominantly observe galaxies in a burst phase, which is likely an observation-bias (Sun et al. 2023). Crucially, the two plots show strong evidence for bursty SFHs based on two different methods: Left: $\text{SFR}_{\text{neb},10}/\text{SFR}_{\text{cont},100}$ traces burstiness using independent information from the nebular Balmer lines and the stellar continuum (similar to estimating the average SFR over 100 Myr time-scales directly from the UV-luminosity); Right: $\text{SFR}_{\text{cont},10}/\text{SFR}_{\text{cont},90}$ traces bursty SFHs self-consistently from the information about the stellar continuum alone. However, in order to confirm the "bursty SFH" scenario, galaxies in mini-quenched phases have to be observed. Observational evidence and a discussion for this is presented in the next subsection.

4.3. Discovery of another (mini-)quenched galaxy at high redshift

In Fig. 11 we present another high-redshift non-, or only weakly, star-forming galaxy with clearly determined redshift of $z = 4.4$, which is in addition to the post-starburst galaxy presented in Strait et al. (2023) and the fully (mini-)quenched galaxy JADES-GS-z7-01-QU in Looser et al. (2023). As in the spectra of those two, we observe a clear $\text{Ly}\alpha$ drop and a weak Balmer break. The stellar continuum of the spectrum is similar to the Strait et al. (2023) object at $z = 5.2$, at slightly lower redshift and with a stellar mass of $M_* = 10^{7.8} M_\odot$. However, as in JADES-GS-z7-01-QU, there is no evidence for ongoing star formation on 10 Myr time-scales, as traced by nebular Balmer emission lines. It should be noted that the stellar mass inferred for JADES-GS-z7-01-QU by our ppxf methodology is $M_* = 10^{8.2} M_\odot$, i.e. ~ 0.5 dex lower than the masses inferred by the other three codes in Looser et al. (2023).

The finding of this additional (mini-)quenched galaxy, supports the scenario in which extreme burstiness can even lead to complete suppression of star formation, at least for short periods of a few 10 Myr.

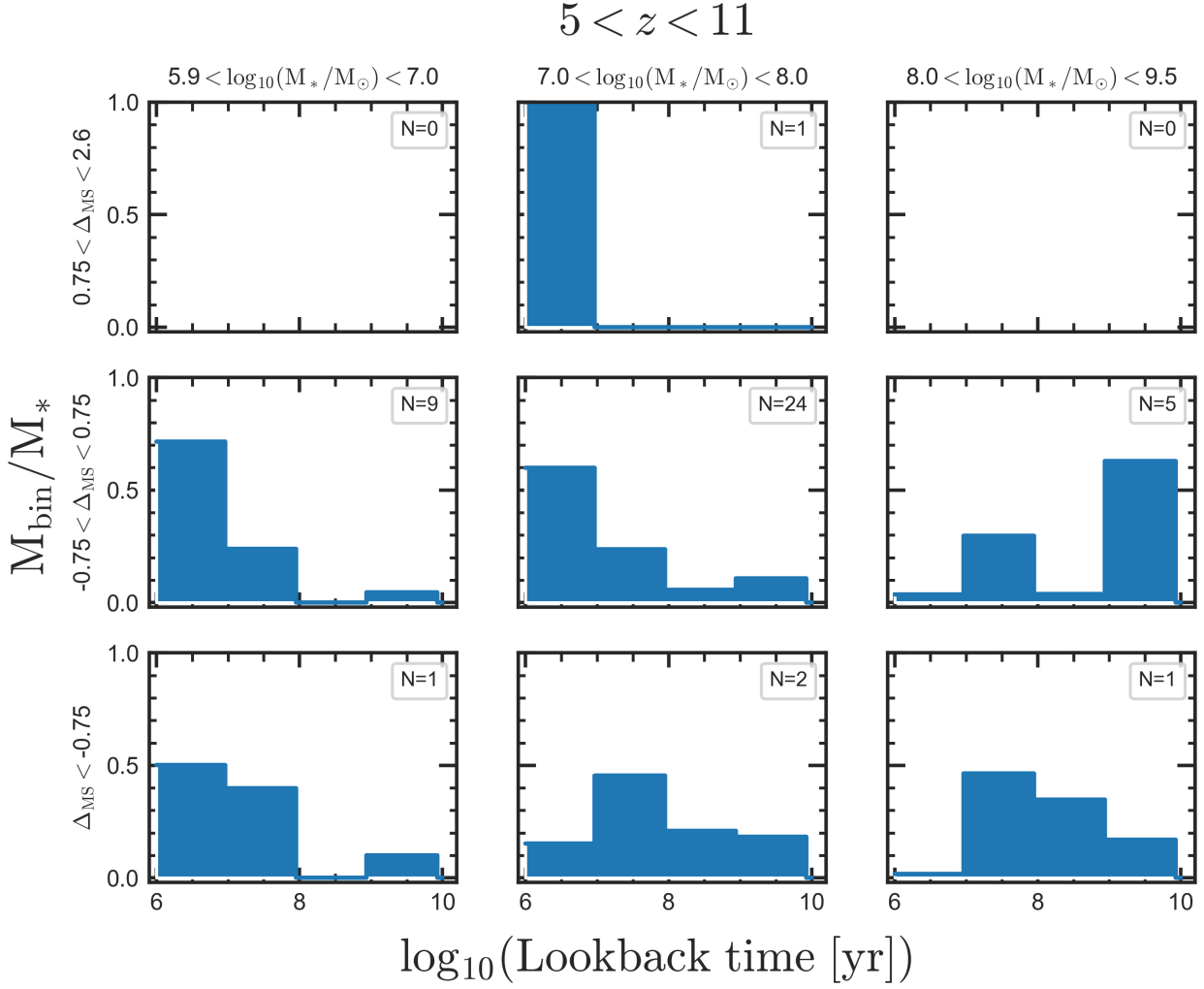


Fig. 5: Mass-weighted stacks of individual "normalized" SFHs of galaxies in three M_* and Δ_{MS} bins for galaxies with redshifts $z > 5$. The number in the legend of each sub-figure indicates the number of galaxies contributing to the stack. See Fig. 3 and section 2.1 for more details.

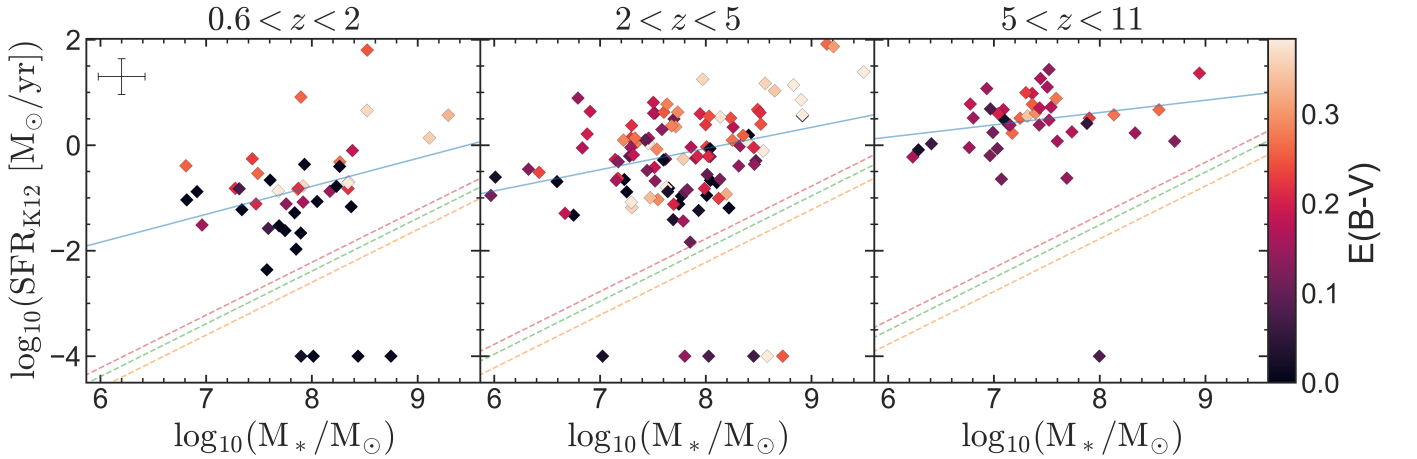


Fig. 6: SFR-mass plane color-coded by reddening $E(B-V)$ of the stellar populations, inferred with PPXF fitting of stellar populations convolved with a Calzetti et al. (1994) dust attenuation law with $E(B-V)$ as a free parameter, in three different redshift bins. Each data-point represents a single galaxy. The quiescent galaxies are plotted at the bottom of the subplots. More details are given in Fig. 2.

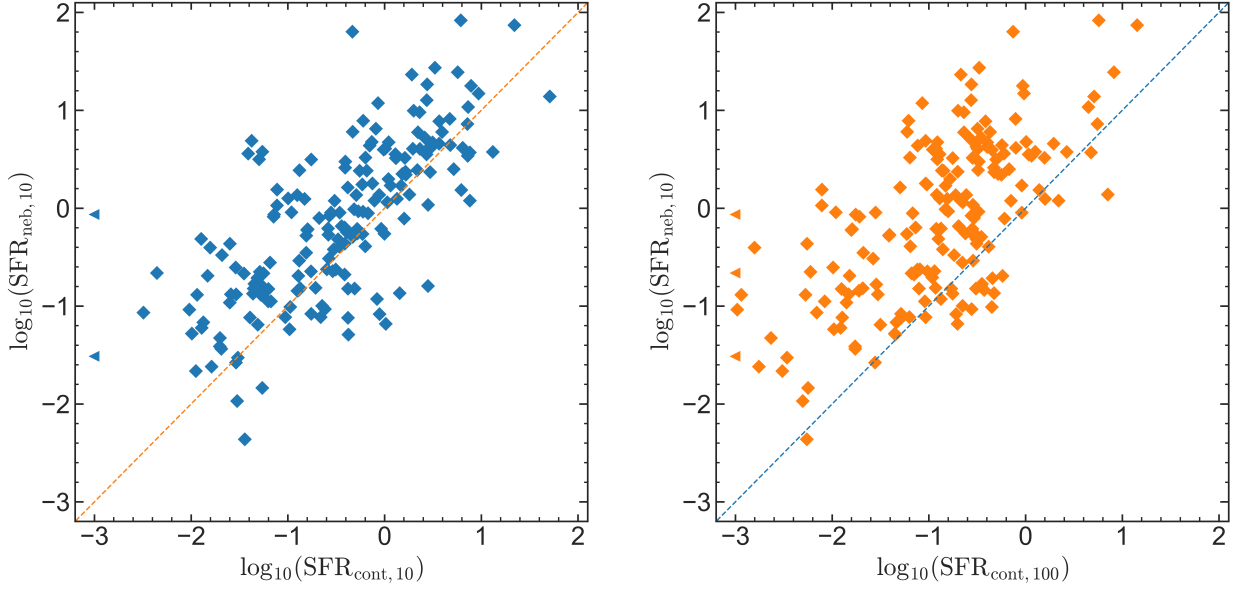
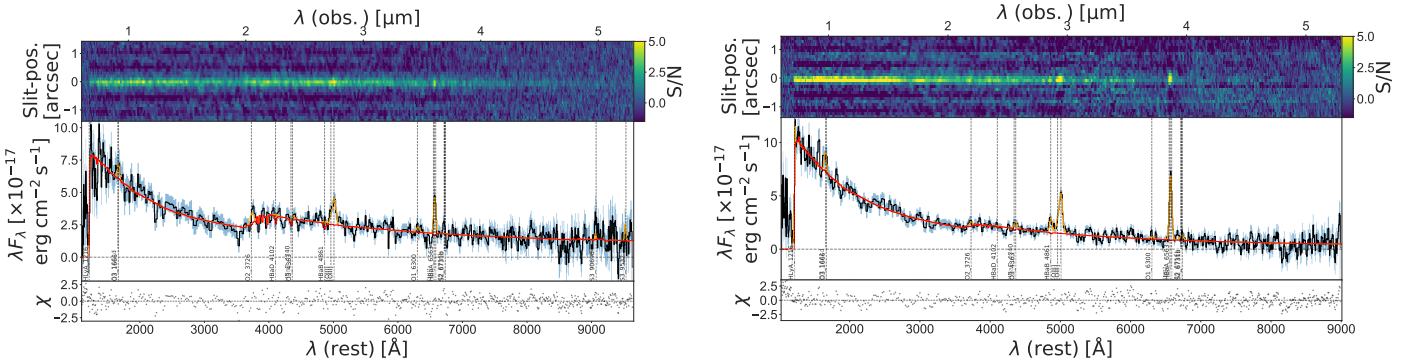


Fig. 7: SFR measured from nebular emission lines, tracing SFR over ~ 10 Myr time-scales, using the K12 relation (y-axis, see section 2.3 for more details) versus SFR measured from the non-parametric stellar population fitting of the continuum with PPXF (x-axis). Left: SFR estimated from stellar population fitting with PPXF averaged over the last 10 Myr before observations. The RMS-scatter between the two measurements is 0.3 dex and we note an offset of 0.2 dex, see text. Right: SFR estimated from stellar population fitting with PPXF averaged over 100 Myr before observations. The interesting question is how much of the scatter and offset between these two quantities stems from noise and measurement uncertainty, and how much comes from physical variability in SFR plus selection bias (see Sun et al. (2023) for a discussion). As we will argue below, a significant portion of the scatter is of physical origin, suggesting bursty SFHs.



(a) Example of a galaxy in a "lull" phase at redshift $z = 4.5$. The spectrum is blue with a quite steep UV slope, but low EW in $H\alpha$, and $[OIII]$ and exhibits a quite strong Balmer break.

(b) Example of a galaxy in a "regular" phase at redshift $z = 4.9$. The spectrum is blue with a steep UV slope, but quite low EW in $H\alpha$, $H\beta$, and $[OIII]$, and exhibits a marginal Balmer break.

Fig. 8: Observational evidence for bursty SFHs in JADES/HST-DEEP. Left: A galaxy in a "lull" phase. Right: A galaxy in a "regular" phase. Both galaxies exhibit low EW in nebular emission lines.

5. Discussion

5.1. Short-timescale SFR from stellar continuum

Our approach to measure SFHs based on PPXF is substantially different compared to Bayesian inference methods (to name only a few, BEAGLE, Chevallard & Charlot 2016; PROSPECTOR, Johnson et al. 2021, BAGPIPES, Carnall et al. 2018; FADO, Gomes & Papaderos 2017; CIGALE, Noll et al. 2009; and PROSPECT, Robotham et al. 2020). To some extent, all these softwares aim to reduce the number of degrees of freedom that determine a galaxy SED by adopting various physically motivated parametrisations and priors. All these assumptions impact the recovered galaxy pa-

rameters (e.g., Carnall et al. 2019a; Leja et al. 2019; Sandles et al. 2022).

Another critical difference between the Bayesian approach and our method is their inclusion of a nebular continuum (which can be substantial in extremely young stellar populations, e.g. Byler et al. 2017; Pappalardo et al. 2021) and of differential dust attenuation (Charlot & Fall 2000).

However, our approach also presents advantages, and has been demonstrated to work both in the local Universe (e.g., Lu et al. 2023; Zhu et al. 2023a,b, Barone et al. 2018, 2021), as well as at redshifts $z \approx 1$ (Cappellari 2022). In particular, we have recently shown how PPXF—without the use of any priors—infers a

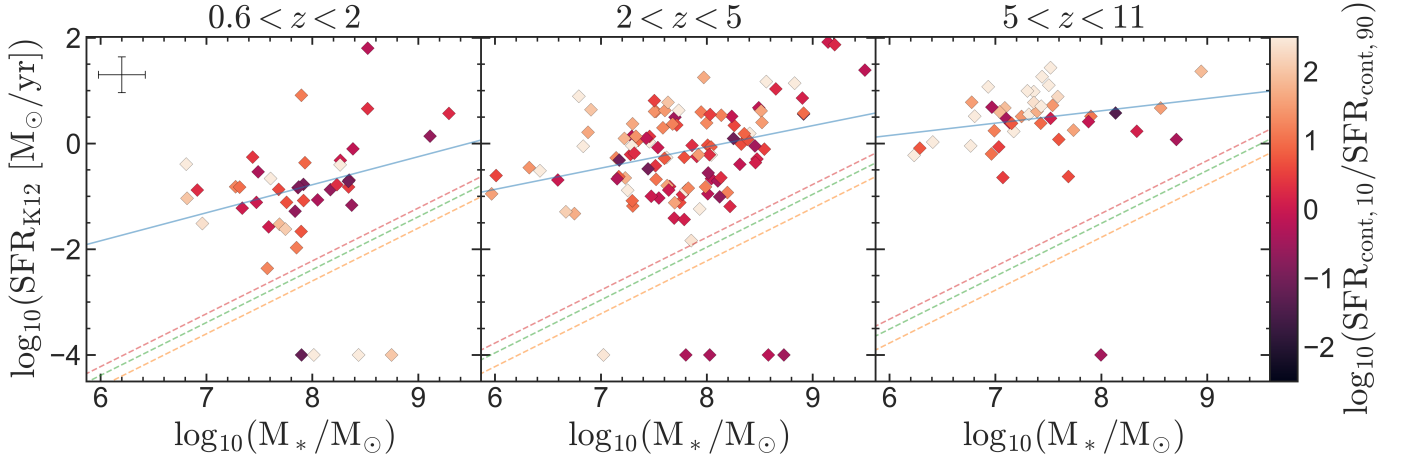


Fig. 9: Observational evidence for bursty SFHs: SFR-mass plane color-coded by the ratio of the SFR over the last 10 Myr ($\text{SFR}_{\text{cont},10}$), and 10 Myr to 100 Myr ($\text{SFR}_{\text{cont},90}$) before the epoch of observation. Both tracers are inferred from non-parametric SSP fitting of the stellar continuum with PPXF. Each data-point represents a single galaxy. The quiescent galaxies are plotted at the bottom of the subplots. More details are given in Fig. 2.

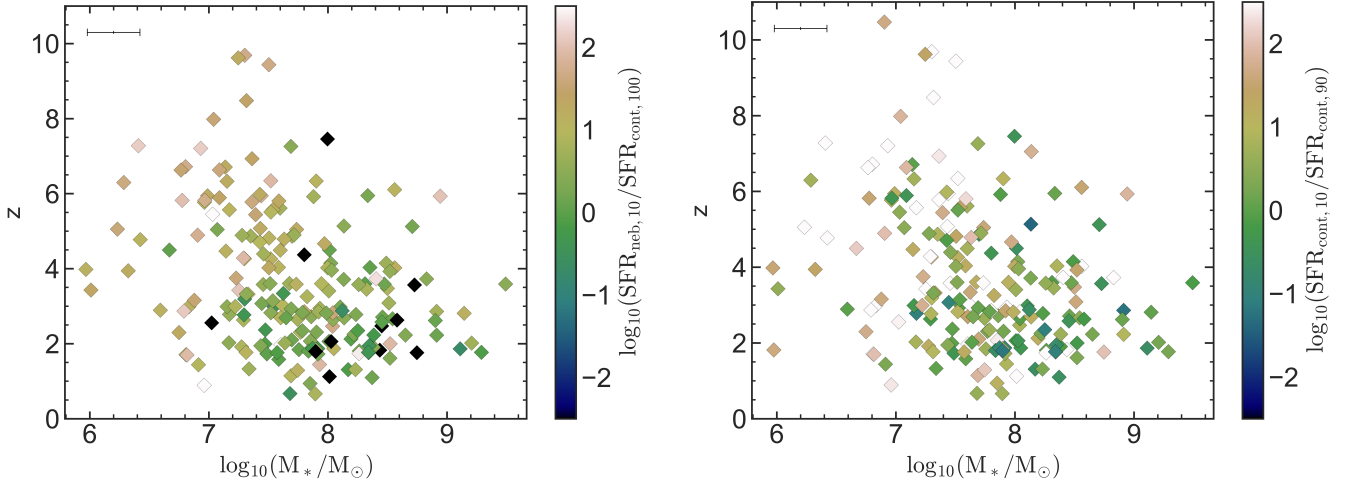


Fig. 10: Stellar mass and redshift dependence of burstiness in galaxy SFHs as inferred from the JADES/HST-DEEP sample. Left: The color-coding indicates the average star-formation over the last ~ 10 Myr, as traced by Balmer emission lines, relative to the average SFR over the last 100 Myr, as traced by the stellar populations. Right: Relative SFRs inferred from the stellar populations; averaged over the last 10 Myr, and 10 Myr to 100 Myr before the epoch of observation (indicated as $\text{SFR}_{\text{cont},10}$ and $\text{SFR}_{\text{cont},90}$ respectively). Green color-coded galaxies are in a regular state at the epoch of observation, white/light galaxies are in a burst, dark galaxies are in a lull, and black galaxies are (mini-)quenched.

realistic chemical-evolution history for local quiescent and star-forming galaxies (Looser et al., submitted).

In addition, and central to this work, we have shown in Fig. 7 that $\text{SFR}_{\text{cont},10}$ is in excellent agreement with $\text{SFR}_{\text{neb},10}$ — even though these two measurements are obtained completely independently. By definition, $\text{SFR}_{\text{cont},10}$ probes the last 10 Myr of the SFH, as inferred through observation of the stellar continuum. $\text{SFR}_{\text{neb},10}$, on the other hand, is based on $\text{H}\alpha$, itself an indirect measure of the ionising continuum. Because this continuum comes from massive stars with lifetimes shorter than 10 Myr, $\text{SFR}_{\text{neb},10}$ probes timescales of 3–10 Myr, comparable to $\text{SFR}_{\text{cont},10}$ (e.g., Kennicutt 1998). The good agreement between these two observables should therefore not be surprising. However, while $\text{SFR}_{\text{cont},10}$ is inferred primarily through the UV continuum redward of $\text{Ly}\alpha$, $\text{SFR}_{\text{neb},10}$ measures the (highly absorbed) UV continuum *blueward* of $\text{Ly}\alpha$. In principle, the correct

SFR could arise ‘for the wrong reason’, e.g., our model neglects both the strong nebular continuum and its suppression due to differential dust attenuation. While we cannot rule out this hypothesis, it seems unlikely that the agreement between $\text{SFR}_{\text{cont},10}$ and $\text{SFR}_{\text{neb},10}$ should arise from two large systematic errors cancelling out.

In the right subplot of Fig. 7 we present a comparison between $\text{SFR}_{\text{neb},10}$ and $\text{SFR}_{\text{cont},100}$, i.e. the average SFR over 100 Myr before the epoch of observation, as inferred from the stellar continuum. This traces the average star-formation activity over the same timescales as empirical tracers based on rest-frame UV emission (e.g. Shivaee et al. 2015). We observe again a strong correlation, but the scatter is much larger than between $\text{SFR}_{\text{neb},10}$ and $\text{SFR}_{\text{cont},10}$. This is already well known, and is commonly interpreted as a measure of star-formation burstiness (e.g., Weisz et al. 2012b).

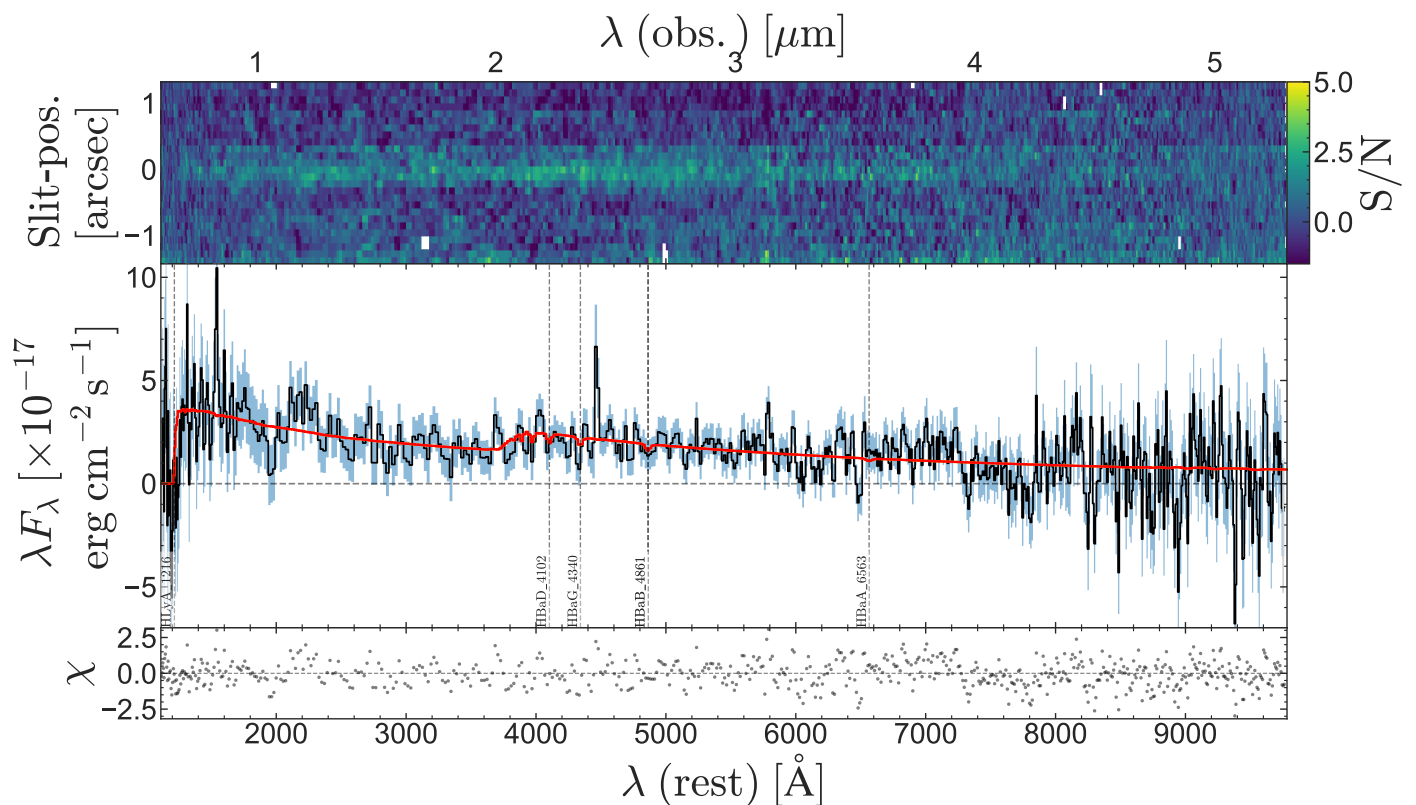


Fig. 11: More spectroscopic evidence for (mini-)quenching at high-redshifts: The Ly α drop and the Balmer break clearly establish the redshift at $z = 4.4$. The absence of emission lines suggests that this galaxy is in a quiescent phase (which is likely only temporarily) and has not formed a significant amount of stars over the last 10 Myr before the epoch of observation.

We note that our SFR indicator may be useful to explore independently galaxy escape fractions f_{esc} . Certain empirical estimators of f_{esc} compare a pair of observables, the equivalent width of recombination lines (e.g., $\text{EW}(\text{H}\beta)$) and the UV slope β to a grid of models. Our method combines the full shape of the UV and visible continuum to infer the amount of stars of various ages. In principle, galaxies with high f_{esc} should manifest as outliers in the $\text{SFR}_{\text{neb},10}$ – $\text{SFR}_{\text{cont},10}$ correlation, with the latter higher proportionally to f_{esc} .

5.2. Stellar population age trends

The trends of stellar age as a function of M_\star , Δ_{MS} and z presented in Fig. 2 provide a first measure of burstiness. A rapidly varying (‘burstier’) SFH would lead to an inconsistent relation between $\text{SFR}_{\text{neb},10}$ and mass-weighted age; for example, galaxies that have stopped forming stars rapidly will have low current $\text{SFR}_{\text{neb},10}$ (thus lying below the MS), but young ages (10–30 Myr), which increases the scatter between Δ_{MS} and age itself for the population as a whole. This seems exactly what we observe in Fig. 2; while most young galaxies (age \approx 10–30 Myr) are on and above the MS, there are several examples of equally young systems below the MS.

Even though the locus of the star-forming MS is likely affected by sample bias, we see large scatter in the SFR of the youngest galaxies, larger than the typical observational uncertainties on SFR itself. However, for the precision of the age measurements, we may be dominated by systematic uncertainties. A comparison with different measurements, e.g., from Bayesian SED modelling, may help quantify what fraction of the observed

scatter about the age– Δ_{MS} relation is intrinsic and what is due to measurement uncertainties.

At the same time, we still observe the clear overall trends of decreasing age with decreasing M_\star , and with increasing z and SFR – which is a reassuring independent test of the quality of our measurements. In particular, the trend of decreasing age with increasing z is not simply due to our truncation of the age grid to match the age of the Universe at the redshift of each galaxy – simply because in each redshift bin, we see systematic age differences across the SFR– M_\star plane. In addition, this trend does not arise from observational bias either: if there were significant numbers of young galaxies below the MS, they would be systematically brighter than older galaxies at the same location on the SFR– M_\star plane.

The trends between age and M_\star and SFR have been observed also in the local Universe ($z < 0.1$; e.g. Looser et al., submitted), where they are interpreted as a manifestation of SFH that self-correlate over the MS timescale $1/\text{sSFR}$ (Looser et al., submitted, Tacchella et al. 2020b). While this timescale is of order few Gyr in the local Universe, at high redshift $1/\text{sSFR}$ is likely much shorter, of order a 100 Myr or even shorter, so the age correlations we observe do not rule out *ipso facto* bursty SFHs.

The overall picture of younger galaxies above the MS, at higher z and lower M_\star agrees with the results we obtain from stacks of individual SFHs in z – M_\star – Δ_{MS} bins (Figs. 3–5). Additionally, stacked SFH appear to show that massive galaxies formed generally earlier and their SFR are on average stationary or declining.

Similarly to what we find for stellar age, also dust reddening trends with M_\star , Δ_{MS} and z (Fig. 6). These trends are qualitatively as one arguably expects: quiescent galaxies and galaxies

below the MS exhibit little or no evidence for dust, whereas star-bursting galaxies have significant reddening. Further, nearly all galaxies at low redshift experience some dust attenuation of the stellar continuum, while we do not observe any highly obscured objects at high- z (this is unlikely to be due to observing bias, but could be due to sample selection bias, see Sandles et al., in prep.). Finally, on average, massive galaxies tend to be dustier than low-mass galaxies. These trends are derived purely from the stellar continuum, but they are in excellent agreement with what we infer from nebular recombination lines (Sandles et al., in prep.) – another independent confirmation of our approach. If we assume dust attenuation roughly traces the amount of cold gas, these trends suggest that SFR and Δ_{MS} are tightly coupled with the availability of fuel. For galaxies in the mass range we explore, this conclusion is in excellent agreement with the prediction of some simulations, which argue the instantaneous Δ_{MS} of a galaxy is driven by rapid gas accretion and depletion, without the ‘dampening’ afforded by large disc reservoirs observed in higher mass galaxies and at lower redshifts (Wang et al. 2019).

5.3. Bursty SFHs

Theoretical models agree that the scatter about the star-forming main sequence increases with increasing z , because the conditions of the primordial Universe are conducive to stronger feedback, which results in galaxies with more ‘bursty’ star-formation histories (Ceverino et al. 2018; Lovell et al. 2022; Ma et al. 2018; Faucher-Giguère 2018; Tacchella et al. 2020a). However, these models differ in how star formation and feedback are implemented, therefore they provide different quantitative predictions. A comparison with observations is particularly useful, because burstiness is predicted both in models with and without AGN feedback, which is thought to also affect the evolution of low-mass galaxies (Koudmani et al. 2019).

Several studies have found prescriptions on how to measure burstiness (e.g., the power spectral density approach of Caplar & Tacchella 2019) and/or how to infer burstiness from observational data (Weisz et al. 2012b; Faisst et al. 2019; Wang et al. 2016; Caplar & Tacchella 2019; Speagle et al. 2014).

However, observational confirmation and characterisation of bursty SFHs is still challenging. The key problem is that burstiness manifests itself as scatter – both about the MS, and between SFR indicators averaged over different timescales. The difficulty is then to extricate the information-laden scatter rooted in physical burstiness from the incidental contribution of measurement noise.

We argue that we overcome this difficulty in two ways. By using a non-parametric approach, we avoid biasing our solutions towards particular SFH shapes. In practice, adding regularisation is akin to introducing a prior, with higher regularisation biasing the solution towards less bursty SFHs. However, this is precisely why we use very low regularisation. Our non-parametric approach increases the accuracy of SFHs, but comes naturally at the cost of decreased precision. However, JADES provides us with the means to overpower low precision measurements; its exceptionally deep spectroscopy, spans both the rest-frame UV and rest-frame optical, i.e., the regions of the spectrum dominated by stellar emission – particularly stars with ages younger than 100 Myr. We use two alternative measures of burstiness, i.e. $\text{SFR}_{\text{neb},10}/\text{SFR}_{\text{cont},100}$ (Fig. 10, left), and $\text{SFR}_{\text{cont},10}/\text{SFR}_{\text{cont},90}$ (Figs. 9 and 10, right)⁵. These are still empirical estimators

⁵ We note that the inferred burstiness does not depend on the χ^2 -value of the fit.

which may be difficult to compare directly to theoretical predictions. However, compared to the classic burstiness measure $\text{SFR}_{\text{neb},10}/\text{SFR}_{\text{UV},100}$, we improve by using the entire information encoded in the spectrum, while $\text{SFR}_{\text{UV},100}$ reduces the SFH in the last 100 Myr to a single, degenerate observable, i.e. UV luminosity.

In the future, it will be crucial to compare our results with Bayesian stellar population modelling codes, which could potentially provide a more physically motivated reconstruction of the star formation history by incorporating complex burst patterns driven by physical expectations. In particular, Bayesian approaches could combine the posterior probability distributions for large samples of galaxies to constrain population-wide parameters like burstiness (e.g. using the hierarchical approach of Wan et al., in prep.).

In section 4, we presented observational evidence for bursty SFHs in high-redshift and in low-mass systems, based on full spectral fitting with `PPXF` (Figs. 9 and 10). Qualitatively, this is in agreement with model expectations. As we mentioned, at fixed stellar mass, galaxies at higher redshift had burstier histories. Conversely, at fixed redshift, burstiness increases with decreasing stellar mass. The physical reason for this burstiness might be different: in high- z galaxies, burstiness is likely a result of abundant amount of cold, dense gas, and high stochasticity of the gas inflow rate combined with powerful supernovae and AGN feedback, while in low-mass galaxies, local star-bursts in short-lived giant molecular clouds might be responsible for the burstiness on short time-scales Tacchella et al. (2020a).

We observe interesting trends with redshift z , Δ_{MS} and M_* : (a) we preferentially observe “bursting” systems (indicated by light colors in Fig. 9) at higher redshift and in low-mass systems, as one can arguably expect from observation bias (Sun et al. 2023). (b) These systems are preferentially situated above the MS, as traced by nebular emission lines, in agreement with the interpretation that they are in a burst phase. (c) Galaxies on the MS are often in a “regular” phase (indicated by red colors). (d) Galaxies below the MS are often in “lull” phases, but also in “regular” phases, which could indicate reduced star formation activity over extended time-scales. (e) High-mass systems are often found in “regular” phases, particularly in the first two redshift bins, suggesting a more regular evolution of these systems – again consistent with theoretical expectations (e.g., Ceverino et al. 2018).

We emphasize that the analysis presented here is a high-redshift view on SFHs. In the local Universe, the SFHs of galaxies are different. Studies of large galaxy samples at redshift $z = 0$ (e.g. MaNGA (Bundy et al. 2015) or SDSS (Abdurro’uf et al. 2022)) show a strong connection between the star-formation activity of a galaxy at the epoch of observation and its past SFH. SFHs of galaxies are steadier, and their evolution is dominated by different physical processes. For example, galaxies dominantly quench through starvation (Peng et al. 2015; Trussler et al. 2020, 2021, Looser et al in prep.), with environment (Peng et al. 2010) or outflows playing a secondary effect. Conversely, our analysis presented here strongly suggests, that SFHs in the young Universe are bursty.

The critical question remains whether the large $\text{SFR}_{\text{cont},10}/\text{SFR}_{\text{cont},90}$ we measure reflects just the tail of a much less bursty, much larger galaxy population. Intriguingly, the complementary approach based on photometry only seems to reach similar conclusions (Endsley et al. 2022, Endsley et al., submitted). Their work uses SED modelling with `BEAGLE` of deep, nine-band NIRC2 imaging from JADES, revealing evidence for “lulling” galaxy candidates.

However, to unambiguously prove the bursty SFH interpretation, galaxies in lull phases and (mini-)quenched galaxies have to be spectroscopically confirmed – which we discuss next.

5.4. Galaxies in "lulls" and (mini-)quenching at high redshift

In section 4.1, we show that the extraordinary depth and data quality of JADES are capable of probing well below the starburst regime. Indeed, we have shown examples of both galaxies on the MS (i.e., "regular" phase, Fig. 8b) as well as below the MS (in "lull" phases; Fig. 8a). We further show that JADES is capable of probing galaxies that are formally below the redshift-dependent quiescent threshold in all three redshift bins (Fig. 2). These galaxies show no evidence for emission lines (Fig. 11 and Looser et al. 2023), and are experiencing (potentially short-lived) phases of quiescence. The fact that these galaxies are present in our sample argues against our findings about burstiness being a result of limited sensitivity. However, the fraction of lull or (mini-)quenched galaxies is clearly lower than that of star-burst systems (Fig. 2). This could ostensibly be the undesired outcome of the initial sample selection, which prioritised objects with high-confidence photometric redshifts. In practice, these amount to galaxies that have stronger broad-band drops, due in turn to either Lyman continuum drop or to high-equivalent-width nebular emission – both of which generally associated with high SFR (Bunker et al., submitted). The difficulty of an unbiased sample selection is highlighted by the complementary approach based on JADES photometry (Endsley et al., submitted), which finds very similar results (i.e., an overabundance of starburst galaxies) based on a NIRC2-selected sample. Indeed, back to our spectroscopic sample, the fact that the only mini-quenched galaxy at $z > 5$ is relatively massive and young ($M_\star = 5 \times 10^8 M_\odot$, 10^8 yr; Looser et al. 2023) suggests that – in this redshift range, we are limited by the depth of JADES. This is again supported by the fact that, in the intermediate-redshift bin, we are able to confirm a mini-quenched galaxy with $M_\star = 8 \times 10^7 M_\odot$ and age $10^{7.9}$ yr – clearly in the low-mass regime where strong feedback is expected to trigger short-lived mini-quenching (Ceverino et al. 2018; Ma et al. 2018; Dome et al. 2023).

According to models, the burstiness of star formation should only increase probing masses $M_\star \approx 10^6 M_\odot$. The galaxies we present here, together with those presented in recent works (Strait et al. 2023; Looser et al. 2023), show that we are finally beginning to probe the obverse face of the burstiness phenomenon. However, a more quantitative understanding will probably require the expensive combination of larger samples and/or even deeper observations. In particular, separating the degenerate effects of mass and redshift will only be feasible with thousands of objects probing effectively the parameter space.

Nonetheless, the analysis presented in this work is strong evidence that galaxies at high-redshift are bursty, and endure these "lulling" and (mini-)quenched phases. In the next section, we discuss the effects of observation bias in more detail.

6. Summary and conclusions

In this work, we combine the non-parametric approach of the PPXF software with the marvellous depth of *JWST*/NIRSpec MSA spectroscopy to offer a view on the star-formation history (SFH) of low- to intermediate-mass galaxies ($10^6 < M_\star < 10^{9.5} M_\odot$) at cosmic dawn, between redshifts $0.6 \lesssim z \lesssim 11$.

The key results of this paper are as follows:

- The correlation of (mass-weighted stellar-population) age with M_\star , z and SFR existed already well before the local Universe and even earlier than Cosmic Noon, at redshifts as high as $5 < z < 11$ (Fig. 2). All else being equal, age increases with increasing M_\star and decreases with increasing z and with increasing distance from the star-forming main sequence, Δ_{MS} . We find consistent trends in the stellar populations in stacks of SFHs in z - M_\star - Δ_{MS} bins. The existence of these correlations is unlikely to result from sample or observation bias, and argues for the SFH of galaxies being correlated on timescales comparable to the main-sequence timescale of $1/\text{sSFR}$ (where sSFR is the specific star-formation rate).
- However, the trends between age, M_\star and SFR, have large scatter, with examples of young stellar populations also below the Main Sequence, which gives a first indication of bursty star formation.
- We introduce and validate a short-timescale, continuum based SFR indicator, averaged over 10 Myr ($\text{SFR}_{\text{cont},10}$). We compare $\text{SFR}_{\text{cont},10}$ to the average over the last 10–100 Myr ($\text{SFR}_{\text{cont},90}$) as an estimate of SFH burstiness.
- By using these parameters, we present additional observational evidence that the SFHs of high-redshift and low-mass galaxies are bursty. Specifically, we use $\text{SFR}_{\text{cont},10}/\text{SFR}_{\text{cont},90}$ to investigate burstiness in the SFR-mass plane and as a function of redshift, and find that high redshift and low-mass galaxies have particularly bursty SFHs, while more massive and lower-redshift systems evolve more steadily.
- We report the discovery of another low-mass galaxy in the fourth phase, which we call: "(mini-)quenched", at redshift $z = 4.4$. This galaxy lies well within the mass regime where numerical simulations predict star-formation being dominated by short and intense bursts. Therefore, the quiescence of this galaxy might be only transient, as discussed in Looser et al. (2023).
- We argue that we see most targets at the observability frontier, i.e. at the highest redshifts and the lowest mass systems, preferentially in "bursting" phases. Their more regular, lulling and (mini-)quenched counterparts are likely at the bottom edge of the observability window at the epoch of observation, even for *JWST*.
- Finally, we use the stellar $E(B-V)$ as a proxy for the amount of dust and find that $E(B-V)$ increases with increasing M_\star and Δ_{MS} , possibly as a result of the correlation between dust and gas mass, and gas mass and SFR in step. We find that $E(B-V)$ decreases at the highest redshifts, although most galaxies at $z > 5$ still have some dust.

However, this is only the beginning of the investigation of stellar populations and bursty SFHs and (mini-)quenching at high redshift with galaxy population samples observed with *JWST*: larger statistical samples of high-S/N galaxy spectra will enable the investigation and quantification of selection effects, which are key to this kind of analysis, and the quantification of various physical aspects of stellar populations and bursty SFHs, like duty cycles, oscillation times, short- and long-term variability, etc., e.g. in the framework of the power spectral density (PSD Tacchella et al. 2020a). And a detailed comparison to numerical cosmological simulations will be crucial to analyse the complex interplay of physical mechanisms contributing to making SFHs bursty. Upcoming observations with *JWST* will provide such a sample, and will continue to reveal the physics processes which shape the observed differing assembly histories of galaxies in the early Universe.

Acknowledgements. TJL, FDE, RM, LS, WB, LS, JS and JW acknowledge support by the Science and Technology Facilities Council (STFC) and by the ERC through Advanced Grant 695671 “QUENCH”. TJL and ALD acknowledge support by the STFC Center for Doctoral Training in data intensive science program. RM also acknowledges funding from a research professorship from the Royal Society. ECL acknowledges support of an STFC Webb Fellowship (ST/W001438/1). SA and BRP acknowledge support from Grant PID2021-127718NB-I00 funded by the Spanish Ministry of Science and Innovation/State Agency of Research (MICIN/AEI/ 10.13039/501100011033). SC acknowledges support by European Union’s HE ERC Starting Grant No. 101040227 - WINGS. AJB, and JC acknowledge funding from the “FirstGalaxies” Advanced Grant from the European Research Council (ERC) under the European Union’s Horizon 2020 research and innovation program (Grant agreement No. 789056). HÜ gratefully acknowledges support by the Isaac Newton Trust and by the Kavli Foundation through a Newton-Kavli Junior Fellowship. JW further acknowledges support from the Fondation MERAC. KB acknowledges support by the Australian Research Council Centre of Excellence for All Sky Astrophysics in 3 Dimensions (ASTRO 3D), through project number CE170100013. The Cosmic Dawn Center (DAWN) is funded by the Danish National Research Foundation under grant no.140. DJE is supported as a Simons Investigator. ALD thanks the Cambridge Harding postgraduate program. DJE BDJ and BER acknowledge support by the JWST/NIRCam contract to the University of Arizona, NAS5-02015. RS acknowledges support from a STFC Ernest Rutherford Fellowship (ST/S004831/1). The research of CCW is supported by NOIRLab, which is managed by the Association of Universities for Research in Astronomy (AURA) under a cooperative agreement with the National Science Foundation.

References

- Abdurro’uf, Accetta, K., Aerts, C., et al. 2022, *ApJS*, 259, 35
- Barone, T. M., D’Eugenio, F., Colless, M., et al. 2018, *ApJ*, 856, 64
- Barone, T. M., D’Eugenio, F., Scott, N., et al. 2021, *arXiv e-prints*, arXiv:2107.01054
- Bruzual, G. & Charlot, S. 2003, *MNRAS*, 344, 1000
- Bundy, K., Bershady, M. A., Law, D. R., et al. 2015, *ApJ*, 798, 7
- Byler, N., Dalcanton, J. J., Conroy, C., & Johnson, B. D. 2017, *ApJ*, 840, 44
- Calzetti, D., Armus, L., Bohlin, R. C., et al. 2000, *ApJ*, 533, 682
- Calzetti, D., Kinney, A. L., & Storchi-Bergmann, T. 1994, *ApJ*, 429, 582
- Cappellari, M. 2017, *MNRAS*, 466, 798
- Cappellari, M. 2022, *arXiv e-prints*, arXiv:2208.14974
- Caputi, K. I., Lagache, G., Yan, L., et al. 2007, *ApJ*, 660, 97
- Carnall, A. C., Leja, J., Johnson, B. D., et al. 2019a, *ApJ*, 873, 44
- Carnall, A. C., McLeod, D. J., McLure, R. J., et al. 2023, *MNRAS*, 520, 3974
- Carnall, A. C., McLure, R. J., Dunlop, J. S., et al. 2019b, *MNRAS*, 490, 417
- Carnall, A. C., McLure, R. J., Dunlop, J. S., & Davé, R. 2018, *MNRAS*, 480, 4379
- Ceverino, D., Hirschmann, M., Klessen, R. S., et al. 2021, *MNRAS*, 504, 4472
- Ceverino, D., Klessen, R. S., & Glover, S. C. O. 2018, *MNRAS*, 480, 4842
- Chabrier, G. 2003, *PASP*, 115, 763
- Charlot, S. & Fall, S. M. 2000, *ApJ*, 539, 718
- Chevallard, J. & Charlot, S. 2016, *MNRAS*, 462, 1415
- Choi, J., Dotter, A., Conroy, C., et al. 2016, *ApJ*, 823, 102
- Conroy, C., Naidu, R. P., Zaritsky, D., et al. 2019, *ApJ*, 887, 237
- Curti, M., Maiolino, R., Carniani, S., et al. 2023, *arXiv e-prints*, arXiv:2304.08516
- Díaz-Santos, T., Armus, L., Charmandaris, V., et al. 2017, *ApJ*, 846, 32
- Dome, T., Tacchella, S., Fialkov, A., et al. 2023, *arXiv e-prints*, arXiv:2305.07066
- Endsley, R., Stark, D. P., Chevallard, J., & Charlot, S. 2021, *MNRAS*, 500, 5229
- Endsley, R., Stark, D. P., Whitler, L., et al. 2022, *arXiv e-prints*, arXiv:2208.14999
- Faisst, A. L., Capak, P. L., Emami, N., Tacchella, S., & Larson, K. L. 2019, *ApJ*, 884, 133
- Faucher-Giguère, C.-A. 2018, *MNRAS*, 473, 3717
- Ferruit, P., Jakobsen, P., Giardino, G., et al. 2022, *A&A*, 661, A81
- Gallazzi, A., Bell, E. F., Zibetti, S., Brinchmann, J., & Kelson, D. D. 2014, *ApJ*, 788, 72
- Gardner, J. P., Mather, J. C., Abbott, R., et al. 2023, *arXiv e-prints*, arXiv:2304.04869
- Gardner, J. P., Mather, J. C., Clampin, M., et al. 2006, *Space Sci. Rev.*, 123, 485
- Gelli, V., Salvadori, S., Ferrara, A., Pallottini, A., & Carniani, S. 2023, *arXiv e-prints*, arXiv:2303.13574
- Giavalisco, M., Ferguson, H. C., Koekemoer, A. M., et al. 2004, *ApJ*, 600, L93
- Gomes, J. M. & Papaderos, P. 2017, *A&A*, 603, A63
- Gordon, K. D., Clayton, G. C., Misselt, K. A., Landolt, A. U., & Wolff, M. J. 2003, *ApJ*, 594, 279
- Jakobsen, P., Ferruit, P., Alves de Oliveira, C., et al. 2022, *A&A*, 661, A80
- Ji, Z. & Giavalisco, M. 2022, *ApJ*, 935, 120
- Ji, Z. & Giavalisco, M. 2023, *ApJ*, 943, 54
- Johnson, B. D., Leja, J., Conroy, C., & Speagle, J. S. 2021, *ApJS*, 254, 22
- Kawata, D. & Gibson, B. K. 2003, *MNRAS*, 346, 135
- Kennicutt, Robert C., J. 1998, *ApJ*, 498, 541
- Kennicutt, R. C. & Evans, N. J. 2012, *ARA&A*, 50, 531
- Koudmani, S., Sijacki, D., Bourne, M. A., & Smith, M. C. 2019, *MNRAS*, 484, 2047
- Leja, J., Carnall, A. C., Johnson, B. D., Conroy, C., & Speagle, J. S. 2019, *ApJ*, 876, 3
- Looser, T. J., D’Eugenio, F., Maiolino, R., et al. 2023, *arXiv e-prints*, arXiv:2302.14155
- Lovell, C. C., Roper, W., Vijayan, A. P., et al. 2022, *arXiv e-prints*, arXiv:2211.07540
- Lu, S., Zhu, K., Cappellari, M., et al. 2023, *arXiv e-prints*, arXiv:2304.11712
- Ma, X., Hopkins, P. F., Garrison-Kimmel, S., et al. 2018, *MNRAS*, 478, 1694
- Maheon, G., Maiolino, R., Curti, M., et al. 2023, *arXiv e-prints*, arXiv:2306.00069
- McLure, R. J., Dunlop, J. S., Cullen, F., et al. 2018, *MNRAS*, 476, 3991
- Noll, S., Burgarella, D., Giovannoli, E., et al. 2009, *A&A*, 507, 1793
- Pacifici, C., Kassin, S. A., Weiner, B. J., et al. 2016, *ApJ*, 832, 79
- Pannella, M., Carilli, C. L., Daddi, E., et al. 2009, *ApJ*, 698, L116
- Pappalardo, C., Cardoso, L. S. M., Michel Gomes, J., et al. 2021, *A&A*, 651, A99
- Peng, Y., Maiolino, R., & Cochrane, R. 2015, *Nature*, 521, 192
- Peng, Y.-j., Lilly, S. J., Kovač, K., et al. 2010, *ApJ*, 721, 193
- Rieke, M. J., Kelly, D. M., Misselt, K., et al. 2023, *PASP*, 135, 028001
- Robotham, A. S. G., Bellstedt, S., Lagos, C. d. P., et al. 2020, *MNRAS*, 495, 905
- Sandles, L., Curtis-Lake, E., Charlot, S., Chevallard, J., & Maiolino, R. 2022, *MNRAS*, 515, 2951
- Shapley, A. E., Sanders, R. L., Reddy, N. A., Topping, M. W., & Brammer, G. B. 2023, *arXiv e-prints*, arXiv:2301.03241
- Shapley, A. E., Sanders, R. L., Salim, S., et al. 2022, *ApJ*, 926, 145
- Shivaei, I., Reddy, N. A., Steidel, C. C., & Shapley, A. E. 2015, *ApJ*, 804, 149
- Smit, R., Bouwens, R. J., Franx, M., et al. 2015, *ApJ*, 801, 122
- Smit, R., Bouwens, R. J., Labbé, I., et al. 2014, *ApJ*, 784, 58
- Speagle, J. S., Steinhardt, C. L., Capak, P. L., & Silverman, J. D. 2014, *ApJS*, 214, 15
- Straat, V., Brammer, G., Muzzin, A., et al. 2023, *arXiv e-prints*, arXiv:2303.11349
- Sun, G., Faucher-Giguère, C.-A., Hayward, C. C., & Shen, X. 2023, *arXiv e-prints*, arXiv:2305.02713
- Tacchella, S., Conroy, C., Faber, S. M., et al. 2022, *ApJ*, 926, 134
- Tacchella, S., Dekel, A., Carollo, C. M., et al. 2016, *MNRAS*, 457, 2790
- Tacchella, S., Forbes, J. C., & Caplar, N. 2020a, *MNRAS*, 497, 698
- Tacchella, S., Forbes, J. C., & Caplar, N. 2020b, *MNRAS*, 497, 698
- Trussler, J., Maiolino, R., Maraston, C., et al. 2020, *MNRAS*, 491, 5406
- Trussler, J., Maiolino, R., Maraston, C., et al. 2021, *MNRAS*, 500, 4469
- Vidal-García, A., Charlot, S., Bruzual, G., & Hubeny, I. 2017, *MNRAS*, 470, 3532
- Wang, E., Lilly, S. J., Pezzulli, G., & Matthee, J. 2019, *ApJ*, 877, 132
- Wang, T., Elbaz, D., Daddi, E., et al. 2016, *ApJ*, 828, 56
- Weisz, D. R., Johnson, B. D., Johnson, L. C., et al. 2012a, *ApJ*, 744, 44
- Weisz, D. R., Johnson, B. D., Johnson, L. C., et al. 2012b, *ApJ*, 744, 44
- Whitaker, K. E., Pope, A., Cybulski, R., et al. 2017, *ApJ*, 850, 208
- Zhu, K., Lu, S., Cappellari, M., et al. 2023a, *arXiv e-prints*, arXiv:2304.11714
- Zhu, K., Lu, S., Cappellari, M., et al. 2023b, *MNRAS*, 522, 6326

¹ Kavli Institute for Cosmology, University of Cambridge, Madingley Road, Cambridge, CB3 0HA, UK

² Cavendish Laboratory, University of Cambridge, 19 JJ Thomson Avenue, Cambridge CB3 0HE, UK

³ Department of Physics and Astronomy, University College London, Gower Street, London WC1E 6BT, UK

⁴ European Southern Observatory, Karl-Schwarzschild-Strasse 2, D-85748 Garching bei Muenchen, Germany

⁵ Centro de Astrobiología (CAB), CSIC-INTA, Cra. de Ajalvir Km. 4, 28850- Torrejón de Ardoz, Madrid, Spain

- ⁶ Department of Physics and Astronomy, University of Manitoba, Winnipeg, MB R3T 2N2, Canada
- ⁷ Cosmic Dawn Center (DAWN), Copenhagen, Denmark
- ⁸ Niels Bohr Institute, University of Copenhagen, Jagtvej 128, DK-2200, Copenhagen, Denmark
- ⁹ Steward Observatory University of Arizona 933 N. Cherry Avenue Tucson AZ 85721 USA
- ¹⁰ School of Physics, University of Melbourne, Parkville 3010, VIC, Australia
- ¹¹ ARC Centre of Excellence for All Sky Astrophysics in 3 Dimensions (ASTRO 3D), Australia
- ¹² Department of Physics, University of Oxford, Denys Wilkinson Building, Keble Road, Oxford OX1 3RH, UK
- ¹³ Scuola Normale Superiore, Piazza dei Cavalieri 7, I-56126 Pisa, Italy
- ¹⁴ Sorbonne Université, CNRS, UMR 7095, Institut d'Astrophysique de Paris, 98 bis bd Arago, 75014 Paris, France
- ¹⁵ Centre for Astrophysics Research, Department of Physics, Astronomy and Mathematics, University of Hertfordshire, Hatfield AL10 9AB, UK
- ¹⁶ Center for Astrophysics | Harvard & Smithsonian, 60 Garden St., Cambridge MA 02138 USA
- ¹⁷ Max-Planck-Institut für Astronomie, Königstuhl 17, D-69117, Heidelberg, Germany
- ¹⁸ AURA for European Space Agency, Space Telescope Science Institute, 3700 San Martin Drive. Baltimore, MD, 21210
- ¹⁹ Department for Astrophysical and Planetary Science, University of Colorado, Boulder, CO 80309, USA
- ²⁰ Department of Astronomy and Astrophysics University of California, Santa Cruz, 1156 High Street, Santa Cruz CA 96054, USA
- ²¹ Astrophysics Research Institute, Liverpool John Moores University, 146 Brownlow Hill, Liverpool L3 5RF, UK
- ²² NSF's National Optical-Infrared Astronomy Research Laboratory, 950 North Cherry Avenue, Tucson, AZ 85719, USA
- ²³ NRC Herzberg, 5071 West Saanich Rd, Victoria, BC V9E 2E7, Canada

Appendix A: PPXF stellar population grid fitting example

To show an illustrative example of our SFH inference methodology based on PPXF, we show the results of the fitting of the spectrum shown in Fig. 1b. In Fig. A.1 the light-weighted 2D grid of SSP-weights is presented, where the age of the SSP templates is given on the x-axis, and the stellar metallicity on the y-axis, respectively. Fig. A.2 shows the conversion of these weights into a non-parametric mass-weighted SFH.

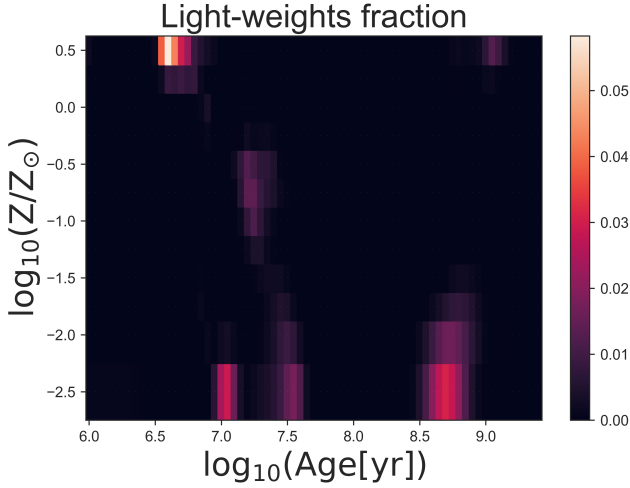


Fig. A.1: Example: PPXF stellar population inference from the spectrum presented in Fig. 1b. The fitted light-weighted SSP age-metallicity grid.

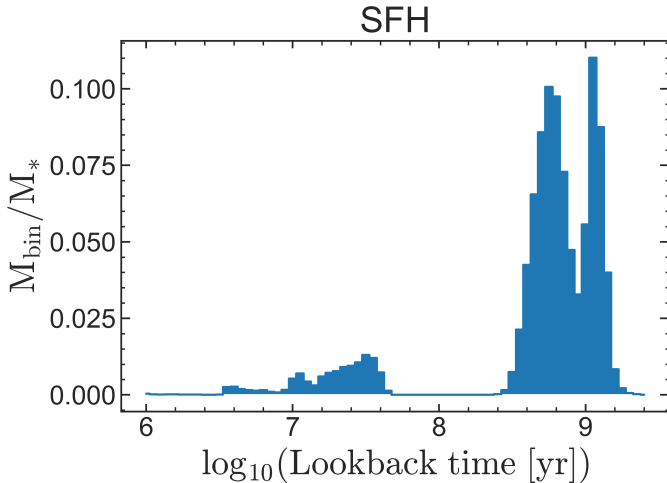


Fig. A.2: Example: PPXF SFH inferred from the spectrum presented in Fig. 1b. The 2D weight-grid (shown in Fig. A.1) converted to a mass-weighted SFH, where the ages of the SSP-templates are equivalent to the star formation activity at that look-back time. The SFH is normalized by the total stellar mass of the galaxy M_* .

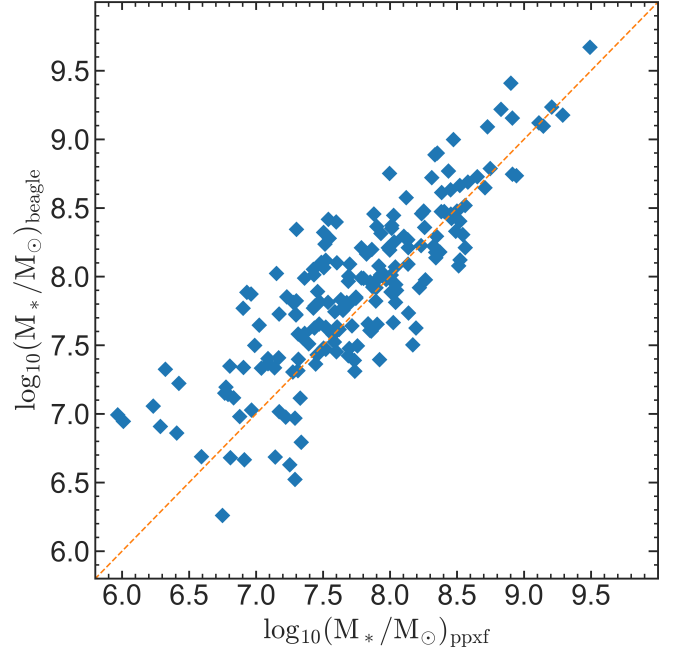


Fig. B.1: Comparison between the stellar masses inferred by PPXF and BEAGLE. The orange line indicates the 1:1 line. The masses show a strong correlation, with an RMS-scatter of 0.2 dex, but exhibit an offset of 0.2 dex.

Appendix B: Comparison between PPXF and BEAGLE stellar mass

In Fig. B.1, we present a comparison between the stellar masses inferred by PPXF, see details in section 2.3, and those inferred by the Bayesian inference code BEAGLE (Chevallard & Charlot 2016). The BEAGLE-derived masses are computed assuming a parametric delayed exponential SFH combined with a 10 Myr burst; and adopting an updated version of the BC03 stellar population model library (Bruzual & Charlot 2003), as described in Vidal-García et al. (2017). More details on the BEAGLE stellar masses for the JADES/HST-DEEP sample are given in Curti et al. (2023) and Chevallard et al. (in prep.). Overall, we find a strong correlation between the stellar masses inferred by the two codes, with a linear fit of $\log_{10}(M_{*,\text{beagle}}) = (0.76 \pm 0.04) \times (\log_{10}(M_{*,\text{ppxf}}) - 8.0) + (8.12 \pm 0.02)$ and a RMS-scatter of 0.2 dex. However, we note a 0.2 dex offset in overall normalisation. The larger masses inferred by BEAGLE compared to PPXF likely stem from the different modelling approaches.